WSKAZÓWKI DOTYCZĄCE PRZYGOTOWANIA ARTYKUŁÓW

- Artykuły przeznaczone do opublikowania w kwartalniku „Technologia i Automatyzacja Montażu" powinny mieć oryginalny i naukowo-techniczny charakter i być zgodne z problematyką czasopisma. Redakcja przyjmuje artykuły w jęz. polskim, jęz. angielskim i jęz. rosyjskim.
- Artykuł o maksymalnej objętości 5 stron A4 wraz z ilustracjami powinien być napisany czcionką Times Roman lub Arial 12 pkt, z interlinią 12 pkt. Formatowany tekst nie powinien mieć podziału na kolumny.
- Tytuł artykułu należy podać w jęz. polskim i jęz. angielskim. Tytuł nieprzekraczający 10 słów powinien odzwierciedlać istotne elementy treści artykułu.
- Struktura artykułów naukowo-technicznych prezentujących prace autora(ów) powinna być następująca: wstęp (wprowadzenie); metodyka (badań, analiz, pracy z podaniem ewentualnie materiałów, założeń itp.); wyniki (badań, analiz); omówienie wyników; wnioski; spis literatury.
- Podpisy pod ilustracjami oraz tytuły tablic należy podać w jęz. artykułu i jęz. angielskim.
- Ilustracje należy dołączyć również jako osobne pliki w formacie: .jpg, .tiff, z rozdzielczością co najmniej 300 dpi. Wszystkie zamieszczane ilustracje powinny być własnością autora(ów) lub należy podać źródło pochodzenia rysunków.
- Wzory matematyczne pisane w edytorze równań Microsoft Equation i powinny być oznaczane kolejnym numerem w nawiasie okrągłym. Wszystkie symbole powinny być objaśnione. Należy stosować jednostki układu SI.
- Spis literatury należy podać w kolejności cytowania w tekście, a odnośniki w tekściepo winny być ponumerowane cyframi arabskimi i umieszczone w nawiasach kwadratowych. W przypadku korzystania z Internetu należy podać adres strony i datę odczytu. Liczbę autocytowań należy ograniczyć do niezbędnych.
- Do artykułu należy dołączyć streszczenie w jęz. artykułu i jęz. angielskim, zawierające minimum 200–250 słów.
- Pod streszczeniem należy podać 3–6 słów kluczowych w jęz. artykułu i jęz. angielskim, zwracając uwagę, by nie były one powtórzeniem tytułu pracy.
- Po spisie literatury zaleca się podanie źródła finansowania pracy.
- Na końcu artykułu należy podać: imiona i nazwiska autorów, tytuły naukowe lub zawodowe, telefon, faks, e-mail, miejsce zatrudnienia wraz z adresem do korespondencji.

PROCEDURA RECENZOWANIA

Procedura recenzowania artykułów w czasopiśmie jest zgodna z zaleceniami Ministerstwa Naukii Szkolnictwa Wyższego zawartymi w opracowaniu „Dobre praktyki w procedurach recenzyjnych w nauce", Warszawa 2011.

Wszystkie artykuły naukowo-techniczne publikowane w kwartalniku „Technologia i Automatyzacja Montażu" są recenzowane.

Nadesłane artykuły są poddawane redakcyjnej ocenie formalnej i otrzymują numer redakcyjny, identyfikujący je na dalszych etapach procesu wydawniczego, a redakcja wysyła do autorów informację o przyjęciu artykułu i wysłaniu go do recenzentów. Do oceny każdej publikacji powołuje się co najmniej dwóch niezależnych recenzentów. Redakcja dobiera recenzentów rzetelnych i kompetentnych w danej dziedzinie. Nadesłane artykuły nie są nigdy wysyłane do recenzentów z tej samej placówki, z której pochodzi autor. Prace recenzentów są poufne i anonimowe. Recenzja musi mieć formę pisemną i kończyć się jednoznacznym wnioskiem o dopuszczeniu artykułu do publikacji w czasopiśmie lub jego odrzuceniu. W przypadku pracy w języku obcym, co najmniej jeden z recenzentów jest afiliowany w instytucji zagranicznej innej niż narodowość autora pracy. Autorzy są informowani o wynikach recenzji oraz otrzymują je do wglądu. W sytuacjach spornych redakcja powołuje dodatkowych recenzentów.

Lista recenzentów publikowana jest w ostatnim zeszycie każdego rocznika.

CONTENTS / W NUMERZE

ANALYSIS OF THE FEASIBILITY OF REPLACING FABRIC SKIN IN HALF-SHELL STRUCTURAL DESIGNS

Analiza możliwości zastąpienia pokrycia płóciennego w konstrukcjach półskorupowych

Sławomir TKACZUK   ORCID 0000-0001-9546-4278
Piotr LESZCZYŃSKI   ORCID 0000-0002-8182-2430
Jarosław DĄBROWSKI

Abstract: One of the many issues associated with aircraft operations is that of structural designs with fabric skin. As one of the solutions addressing these problems, this paper proposes replacing the existing fabric skin with a new covering made of a composite material. The object of analysis available to the authors was a horizontal stabilizer of Mi-2 helicopter. This paper presents the results of fatigue tests applied to the thin-walled structure of the horizontal stabilizer, carried out under two scenarios: (I) with the fabric skin removed and (II) with the composite material skin installed. During the tests, strain values were measured at selected points of the stabilizer structure, using linear type resistance strain gauges and in a rectangular rosette arrangement. The test results confirmed the feasibility of replacing the fabric skin with a composite material skin.

Keywords: aircraft, fabric skin, composite material skin, fatigue testing, strain measurement

Streszczenie: Jednym z wielu zagadnień związanych z eksploatacją statków powietrznych są problemy dotyczące zespołów konstrukcyjnych posiadających płócienne pokrycie. Jako jedno z rozwiązań tych problemów, w artykule zaproponowano zastąpienie dotychczasowego pokrycia płóciennego nowym pokryciem w postaci materiału kompozytowego. Obiektem analizy, jakim dysponowali autorzy był statecznik poziomy śmigłowca Mi-2. W artykule przedstawiono rezultaty badań zmęczeniowych cienkościennej struktury tego statecznika poziomego, przeprowadzone dla dwóch przypadków: (I) z usuniętym pokryciem płóciennym oraz (II) z zamontowanym pokryciem kompozytowym. Podczas badań dokonywano pomiaru wartości odkształceń w wybranych punktach struktury statecznika, z wykorzystaniem tensometrów oporowych typu liniowego oraz w układzie rozety prostokątnej. Wyniki badań potwierdziły możliwość zastąpienia pokrycia płóciennego pokryciem kompozytowym.

Słowa kluczowe: statek powietrzny, pokrycie płócienne, pokrycie kompozytowe, badania zmęczeniowe, pomiar odkształceń

Introduction

Airframes of aircraft are most often manufactured as half-shell structures [1,2,11]. A characteristic feature of such structures is that individual airframe components are made of metal, mainly aluminum alloys. Due to the type of materials, riveting is the most common method of making connections. However, despite the passage of time, aircraft whose assemblies - primarily the stabilizers - are made as half-shell structures with fabric skin are still in service.

Fabric was used extensively in truss airframes due to the fact that it was the only material available that was suitable for use as a skin due to its density. The passage of time caused the number of aircraft with fabric skin to decline steadily, limiting the use of fabric to special aircraft, vintage aircraft and gliders, etc. [4] At the same time, this caused a drastic decrease in qualified personnel whose skills would allow them to perform work related to the replacement of fabric skin, or repair their damage. Against all appearances, replacing the skin is a very tedious and complicated process that also requires manual

skills from the contractors. Fabric skin also requires exercising care during aircraft operation, as it can be easily damaged (e.g., torn). Fabric skin exposed to external factors, i.e. UV light, moisture, dust and even biological agents (moulds and algae), age quickly and need to be replaced.

Recognizing the problems associated with the operation of airframe assemblies covered with fabric, especially given the absence of personnel and time-consuming replacements, it was decided to see if it was possible to replace the fabric skin with another material, i.e. composite material.

Test object

A typical example of a metal, half-shell structure with a single-circuit caisson with a skin that is flexible (made of fabric) outside the caisson is the horizontal stabilizer of the Mi-2 helicopter (Fig.1). Therefore, it was decided to use this team to study the feasibility of a new skin material [7].
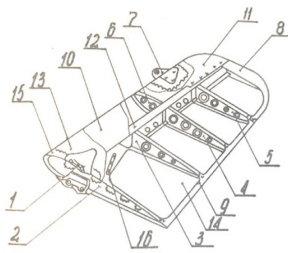
Fig. 1. Stabilizer design [7] [Photo S.Tkaczuk]: 1- cover plate; 2- rib No. 1; 3- rib No. 2; 4- rib No. 3; 5- rib No. 4; 6- rib No. 3; 7- pylon; 8- section; 9- rear strip; 10- metal skin; 11-terminal fairing; 12-truss; 3,14- fabric skin; 15- percale band; 16-countersunk rivet

Analyzing the design of the stabilizer and the method of connecting the fabric to the framework, a simple replacement of the fabric with aluminum alloy sheeting was ruled out. This was not possible due to the design of the rib racks preventing the use of rivets to connect the covering to the rib.

A proposal was made to replace the fabric with a composite material and in the the first phase of work an sandwich structure of glass composite and Herex foam was used. Glass composite has properties similar to those of fabric skin - it is strong and flexible.

The composite material skin (Fig. 2) was made as a single component consisting of an upper and lower

Fig. 2. The top plate of the stabilizer cover and the interior of the new stabilizer cover [Photo S. Tkaczuk]

covering plate and a runoff element connecting the two plates into a single unit. Each cover plate consists of two layers of E91 glass fabric infused with resin, with Herex foam sandwiched between them - resulting in a sandwich design [3]. The application of foam was intended to make the cover plates rigid in the rib spacing. The base in the composite material was LR285 epoxy resin + H285 hardener [6].

The covering element prepared in this way was glued to the stabilizer skeleton. The component was glued directly to the caisson plate and racks of rib No. 1 and the trailing edge, while for the other ribs, i.e., No. 2, No. 3, and No. 4, were glued through the composite cladding with which they were previously covered. In addition, along the edge of the caisson at the height of each rib, the composite element was riveted with one-sided rivets

Experimental tests

Considering the load fatigue of helicopter airframes, the study was limited to fatigue tests comparing the stabilizer strain without and with a composite skin after a specified number of fatigue cycles.

• **Measurement system**

It was decided to perform strength tests of the horizontal stabilizer without skin and with a glued composite element replacing the fabric skin.

The scope of the test was to perform 500,000 load cycles with a displacement of 4.5 mm (equivalent to a force of 1.25 kN) and a frequency of 0.42 Hz. The assumed load value corresponded to the value of the aerodynamic force generated by the horizontal stabilizer [10] calculated for a Mi-2 helicopter flying at 190 km/h [12].

The fatigue tests were conducted on a fatigue test bench consisting of a loading system and a strain gauge bridge system with a CL 460 multi-channel recorder for recording measurements from the resistance strain
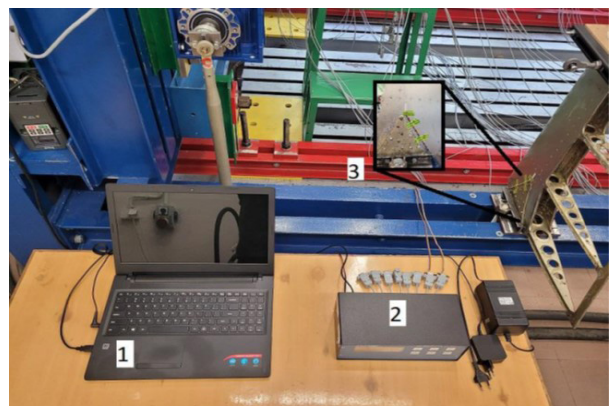
Fig. 3. Test bench [Photo by S. Tkaczuk]
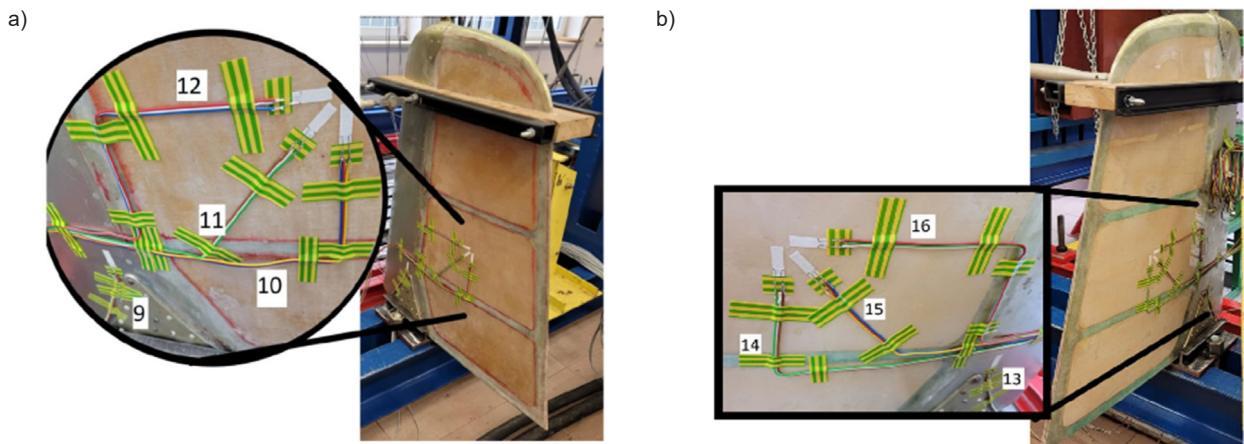
Fig. 4. Distribution of strain gauges on the skin: a) top skin, b) bottom skin [Photo. S. Tkaczuk]

gauge system. The elements of the test bench discussed are shown in Figure 3.

The strain gauges were placed on both sides of the stabilizer: in a linear arrangement on the surface of the caisson's cover plate (at the height of the truss wall) and in a rectangular arrangement, in the center of the area between ribs No. 2 and No. 3 (Fig. 4) [9].

Measurements were take under two scenarios: I) load on the structure with the fabric skin removed and II) load on the structure with the composite skin installed.

Scenario I. Loading of the structure with the fabric skin removed

Test conditions:

During this test, the oscillations of the stabilizer were investigated in a zero pulsating cycle, i.e. the value of deviation from the neutral position was +4.5 mm (Fig. 5). Channel 13 refers to the strain gauge on the lower surface of the stabilizer, while Channel 9 indicates the values read by the strain gauge compressed on the upper surface of the stabilizer (Table 1).

Table 1. Strain registration parameters for the initial 0 cycles - before the start of the fatigue test [own analysis]

	Bottom stabilizer surface	Top stabilizer surface
	Channel 13	Channel 9
Min. value. [μm/m]	-20	-477
Max. value. [μm/m]	501	19
Registration of duration period [s]	77.4	77.4
No. of samples	872	872
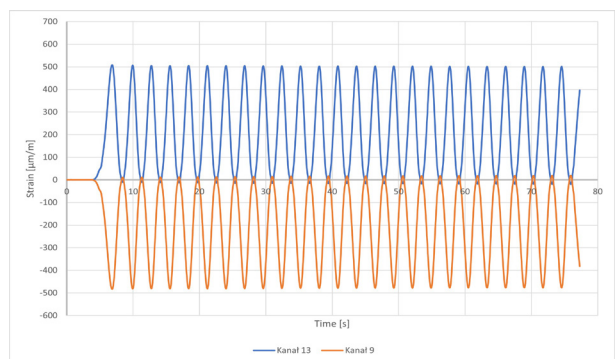
Fig. 5. Diagram of strain changes over time: Channel 9 - strain gauge on the top surface of the stabilizer, Channel 13 - strain gauge on the bottom surface of the stabilizer [own analysis]

Scenario 2. Loading of structure with composite skin installed.

Strain gauge measurements

In this fatigue test, channels numbered 9 through 12 of the CL460 Multi-Channel recorder corresponded to strain gauges on the upper surface of the stabilizer, while channels numbered 13 through 16 indicated the values read by the strain gauges on the lower surface of the stabilizer.

Measurement results

Not knowing exactly how the new composite skin under test would behave during the test, such as whether localised peeling would occur from the dural framework of the stabilizer, the entire test was divided into stages of 50,000 cycles each. After the completion of each such step, strain values were recorded for all eight (8) strain gauges [8].

As examples, Table 2 shows the recorded parameters for a run of 0 cycles, while Table 3 shows the recorded parameters for a run of 500,000 cycles. The waveforms

Table 2. Strain registration parameters for the initial 0 cycles - before the start of the fatigue test [own analysis]

Measurement case	Top stabilizer surface					Bottom stabilizer surface				
	I.	II.				I.	II.			
Channel No.	9	9	10	11	12	13	13	14	15	16
min. [µm/m]	-477	-522	-100	-470	-55	-20	-5	-13	-19	-13
max. [µm/m]	19	3	-9	-5	-7	501	539	368	659	157
Registration of duration period [s]	77.4	61.8	61.8	61.8	61.8	77.4	61.8	61.8	61.8	61.8
Value in absolute terms [µm/m]	496	525	91	465	48	521	544	381	678	170

Table 3. Parameters for recording strains for 500,000 cycles – after completion of the fatigue test [own analysis]

Measurement case	Top stabilizer surface					Bottom stabilizer surface				
	I.	II.				I.	II.			
Channel No.	9	9	10	11	12	13	13	14	15	16
min. [µm/m]	-477	-334	-16	32	-1	-20	-398	-18	0	0
max. [µm/m]	19	145	58	479	54	501	86	336	619	73
Registration of duration period [s]	77.4	61.4	61.4	61.4	61.4	77.4	61.4	61.4	61.4	61.4
Value in absolute terms [µm/m]	496	479	74	447	55	521	484	354	619	73

for the number of cycles 0 and 500,000 are shown in Figures 6 and 7.

A comparison of the results obtained on Channels 9 and 13 (Table 2 and Table 3) shows that the absolute values of the measurements made for both measurement cases analyzed are of the same order. For this type of strain gauge measurement, differences in readings as small as tens of µm/m are treated as insignificant because they occur at the fifth decimal place. The results obtained allow us to conclude that the use of composite as skin of the tested stabilizer did not change the values of deformation of the structure. Comparing the strain values recorded at the beginning of the fatigue test (for 0 cycles) with the strain values measured after the end of the test (for 500,000 cycles), there were also no significant differences in the strain values (Table 2 and Table 3).
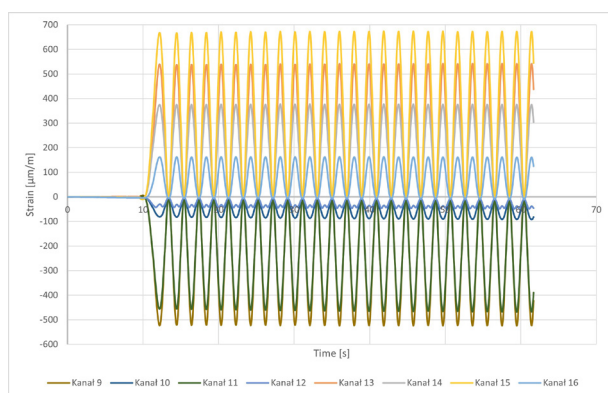
Fig. 6. Graph of strain changes over time for the initial 0 cycles - before fatigue testing: Channels 9-12 - strain gauges on the top surface of the stabilizer, Channels 13-16 - strain gauges on the bottom surface of the stabilizer
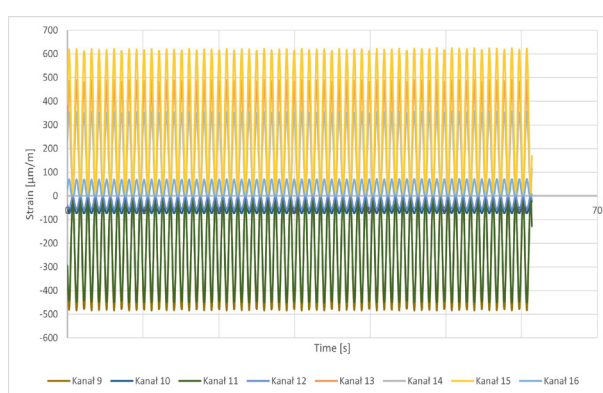
Fig. 7. Graph of strain changes over time for the final 500,000 cycles - after the end of the fatigue test: Channels 9-12 - strain gauges on the top surface of the stabilizer, Channels 13-16 - strain gauges on the bottom surface of the stabilizer

Major strains

From the strain values measured by rectangular strain gauge rosettes, for each stage of 50,000 fatigue cycles, the maximum and minimum major strains, expressed by the following formulas (1) (2) [5], were calculated:

$$\varepsilon_{max} = \frac{\varepsilon_0 + \varepsilon_{90}}{2} + \frac{\sqrt{2}}{2} \cdot \sqrt{(\varepsilon_0 - \varepsilon_{45})^2 + (\varepsilon_{45} - \varepsilon_{90})^2} \tag{1}$$

$$\varepsilon_{min} = \frac{\varepsilon_0 + \varepsilon_{90}}{2} - \frac{\sqrt{2}}{2} \cdot \sqrt{(\varepsilon_0 - \varepsilon_{45})^2 + (\varepsilon_{45} - \varepsilon_{90})^2} \tag{2}$$
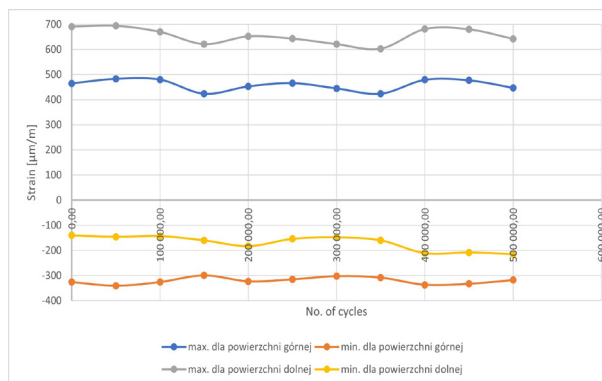
Fig. 8. Values of maximum and minimum major strains

Table 4. Values of maximum and minimum major strains for successive stages of fatigue testing [own analysis]

	Major strains			
	Top surface of stabilizer		Bottom surface of stabilizer	
No. of cycles	max. [μm/m]	min. [μm/m]	max. [μm/m]	min. [μm/m]
0	465	-326	691	-140
50.000	483	-341	694	-146
100.000	480	-326	670	-143
150.000	424	-299	621	-160
200.000	453	-323	652	-183
250.000	466	-315	643	-154
300.000	445	-302	621	-148
350.000	424	-308	603	-160
400.000	479	-337	681	-211
450.000	477	-333	680	-208
500.000	447	-318	642	-215

The results of these calculations are shown in Table 4.

The results collected in Table 4 are presented graphically in the summary Figure 8. The figure shows the maximum and minimum values of the calculated major strains. The values of maximum major strains were recorded on the skin of the bottom surface of the stabilizer in tension, whereas the values of minimum major strains were recorded on the skin of the top surface of the stabilizer in compression.

Conclusions

Based on the obtained results of fatigue tests of the horizontal stabilizer of Mi-2 helicopter, it was concluded that:

1. The use of a skin made of glass composite reinforced with Herex spacer did not enhance the rigidity of the stabilizer.
2. The results obtained during the carried out tests fully confirmed an option of replacing thefabric skin with a composite material skin.
3. There was no increase in the strain values of the skin itself compared to the strain values measured prior to the fatigue tests.
4. If the fabric skin was replaced with a composite material skin, the service life of this structural assembly would probably be extended. However, the authors of this paper are unable at this stage to determine precisely by how many calendar years or operational hours.

References

[1] Danilecki S. 2016. Konstruowanie samolotów. Wyznaczanie obciążeń. Warszawa: Wojskowa Akademia Techniczna.

[2] Danilecki S. 2018. Projektowanie samolotów. Warszawa: Wojskowa Akademia Techniczna.

[3] Godzimirski J., J. Kozakiewicz, J. Łunarski, W. Zielecki. 1997. Konstrukcyjne połączenia klejowe elementów metalowych w budowie maszyn. Rzeszów: Oficyna Wydawnicza Politechniki Rzeszowskiej.

[4] Jach M. 2005. Budowa płatowców. Skrypt Aeroklubu Łódzkiego. Łódź: Aeroklub Łódzki.

[5] Jankowski L. 2015. Tensometria rezystancyjna. Wrocław: Wydawnictwo Politechniki Wrocławskiej.

[6] Komorek A., P. Przybyłek, R. Szczepaniak, M. Rośkowicz. 2019. "The Effect of Low Energy Impact Loads on the Flexural Strength of a Sandwich-Structured Composite with Herex Core". 36th Danubia-Adria Symposium on Advances in Experimental Mechanics. 24-27 September 2019. Pilzno, Czech Republic.

[7] Ministerstwo Obrony Narodowej. 1972. Śmigłowiec Mi-2. Opis techniczny. Płatowiec. Poznań: MON.

[8] Ochelski S. 2004. Metody doświadczalne mechaniki kompozytów konstrukcyjnych. Warszawa: Wydawnictwo Naukowo-Techniczne.

[9] Roliński Z. 1981. Tensometria oporowa: podstawy teoretyczne i przykłady zastosowań. Warszawa: Wydawnictwo Naukowo-Techniczne.

[10] Sobieraj W. 2014. Aerodynamika. Warszawa: Wojskowa Akademia Techniczna.

[11] Witkowski R. 1998. Wprowadzenie do wiedzy o śmigłowcach. Warszawa: Biblioteka Naukowa Instytutu Lotnictwa.

[12] Wytwórnia Sprzętu Komunikacyjnego Świdnik. 1977. Śmigłowiec Mi-2. Instrukcja użytkowania w locie. Świdnik: WSK.

Sławomir Tkaczuk, Ph.D., Eng.,
e-mail: slawomir.tkaczuk@wat.edu.pl

Piotr Leszczyński Ph.D., Eng.,
e-mail: piotr.leszczynski@wat.edu.pl – correspondence author

Jarosław Dąbrowski, Military University of Technology (MUT) Faculty of the Mechatronics, Armaments and Aerospace, Institute of Aviation Technology
ul. gen. Sylwestra Kaliskiego 2
00-908 Warsaw 46

COMPARISON OF SURFACE TOPOGRAPHY AFTER LENS-SHAPE END MILL AND BALL ENDMILL MACHINING

Porównanie topografii powierzchni po obróbce frezem soczewkowym oraz kulistym

Piotr ŻUREK   ORCID 0000-0002-8735-6426
Karol ŻURAWSKI   ORCID 0000-0002-7898-2628
Artur SZAJNA   ORCID 0000-0002-3820-7272
Rafał FLEJSZAR   ORCID 0000-0001-5231-6494
Marcin SAŁATA   ORCID 0000-0002-2338-4380

A b s t r a c t: The article presents the results of comparative investigations concerning surface topography obtained as a result of machining the workpiece with ball end and lens-shape end mills. The analysis was conducted for various values of width of cutting ae and feed speed fz. The research results include the comparison of surface topography maps and parameters of linear and surface roughness. It was shown. as a result of the research. that the use of lens-shape end mill allows to obtain similar values of surface topography parameters to the obtained values in machining with ball end mill. while achieving more than twice the efficiency of machining. As a result. there was demonstrated the potential for the use of lens-shape end mills in finishing operations as a useful alternative to ball end mills.

K e y w o r d s: lens-shape end mill. barrel end mill. ball end mill. surface topography. surface roughness

S t r e s z c z e n i e: W artykule przedstawiono wyniki badań porównawczych topografii powierzchni uzyskanych po obróbce przedmiotu frezem kulistym oraz soczewkowym. Analizę przeprowadzono dla różnych wartości szerokości skrawania a_e oraz prędkości posuwu f_z. Wyniki badań obejmują porównanie map topografii powierzchni oraz parametrów chropowatości. liniowych i powierzchniowych. W wyniku badań wykazano. że zastosowanie freza soczewkowego pozwala na uzyskanie zbliżonych wartości parametrów topografii powierzchni jak po obróbce fezem kulistym. osiągając przy tym ponad dwa razy większą wydajność obróbki. W rezultacie wykazano potencjał zastosowania frezów soczewkowych w operacjach wykończeniowych jako użytecznej alternatywy dla narzędzi kulistych.

S ł o w a k l u c z o w e: frez soczewkowy. frez baryłkowy. frez kulisty. topografia powierzchni. chropowatość powierzchni

Introduction

Currently. the five-axis milling method is widely used in the production of components with complex geometry in many branches of industry. Thanks to its flexibility. this technology found its success in the production of parts for several industries like aviation. automotive. tool. energy and medical industries. Additionally. five-axis milling is subject to increasing expectations both in terms of dimensional accuracy and surface quality of manufactured products.

In the case of finishing machining freeform surfaces. the types of mills with the widest use are the ball end mills (Fig. 1a). Their main advantage is a wide range of applicability in relation to the shape of the machined surface and easy gen-eration of tool paths. However. the machining process using ball end mills shows a has a very low efficiency due to the large quantity of tool paths required [4–7] .

The popularity of ball end mills is reflected in a very large number of scientific studies. The issues related to the mechanics and dynamics of the process were taken
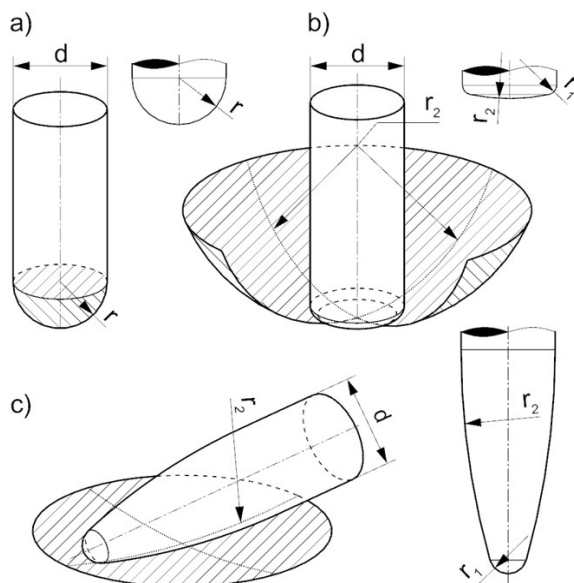

Fig. 1. Diagram of: a) ball end mill ($d = 2 \cdot r$). b) lens-shape end mill ($d << 2 \cdot r_2$). c) oval-form end mill ($d << 2 \cdot r_2$)

up by Altinas et al. [1, 8]. In their work. they developed a mathematical description of the geometry of the ball end milling cutter and model of the cutting layer cross-section as well as proposed mechanistic equations for the components of the cutting force.

Larue. Ferry et al. [9, 10, 12] extended the analysis with the peripheral milling. Moreover, Wojciechowski [22] proposed a model of the components of the cutting force. vibration. deformation and tool wear when machininghardened steels. Additionally. Ghorbani et al. [11] included the values of the principal curvatures of the machined freeform surface and the values of the radial runout of the mill in the cutting force model.

The subject of surface topography obtained after machining with a ball end mill was discussed by Arizmendi et al. [2]. They proposed an analytical model for determining the surface topography after machining with a ball end mill based on the trajectory of the cutting edge movement. taking into account technological parameters such as tool feed. cutting depth. cutting width and tool radial runout. Moreover. Seyed Ehsan et al. [15] continued the issue for the case of five-axis machining. They proposed a method for determining the surface topography in which the position of the tool axis was taken into account by defining the lead and tilt angles.

Due to the intensive development of CAM software. it is becoming more frequent to use the tools with unusual shapes. Circle segment end mills are gaining more and more popularity. especially in the finishing of freeform surfaces. The geometry of these tools is defined by an arc. whose radius r_2 is many times greater than the radius of the tool shank $d/2$ [24. 25]. This solution makes possible maintaining the desired surface quality. while significantly reducing the number of tool paths. However. the main disadvantage of that type of tools is the limited positioning range in relation to the machined surface [4–7].

Scientific studies concerning the circle segment end mills most often put their focus on barrel-shape and oval form tools. Artrxe. Urbikain et al. [3] presented a mathematical description of the geometry of an oval form endmill and proposed a mechanistic model of cutting force components with reference to the radial runout of the tool. In subsequent works [16, 17, 19] the model was developed further by analysing the influence of the lead angle. tilt angle and vibrations on the distribution of cutting force components. This issue was also developed for barrel-shape tools in the work of Olver et al. [14].

Urbikan et al. [18, 20] presented a mathematical and empirical models for the determination of surface roughness after machining with an oval form and a barrel-shape mill. The issues of positioning and generating a tool path of the barrel-shapeend mills were taken up in the work of Wang et al. [21]. YaoAn et al. [23] and Ming et al. [13]. Each of the works presents different algorithms for determining the position of the tool axis and points of contact with the machined surface in the case of peripheral milling.

One type of circle-segment end tools is the lens-shape end mill. Despite theavailabilityof the solution of this type of mills offered by tool manufacturers. there is no scientific literature on this subject. The aim of this study is to demonstrate the applicability of lens-shape end mills as an alternative to ball end mills in five-axis finishing milling operations.

Materials and methods

The first stage of the research was to perform a finishing operation of the test workpiece. consisting of a surface divided into 16 areas (Fig. 3). Different values of the path width b_r and the tool feedrate v_f were used for each of 16 machined areas. Tests numbered 1 – 8 were carried out with a EMUGE FRANKEN 3544L.10020A lens-shape end mill with a radius of $r_2 = 40$ [mm] (Fig. 2a). while tests numbered 9 –16 were performed using a Sandvik Coromant R216.42-10030-AC19P 1620 ball end mill with a radius $r = 5$ [mm] (Fig. 2b). Both tools were mounted in a Sandvik Coromant 930-HA06-HD-20-104 holder with the same overhang equal to 37 [mm].
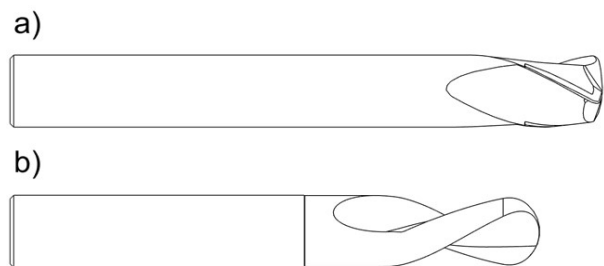
Fig. 2. Tools used for tests a) lens-shape end mill EMUGE FRANKEN 3544L.10020A b) ball end mill Sandvik Coromant R216.42-10030-AC19P 1620
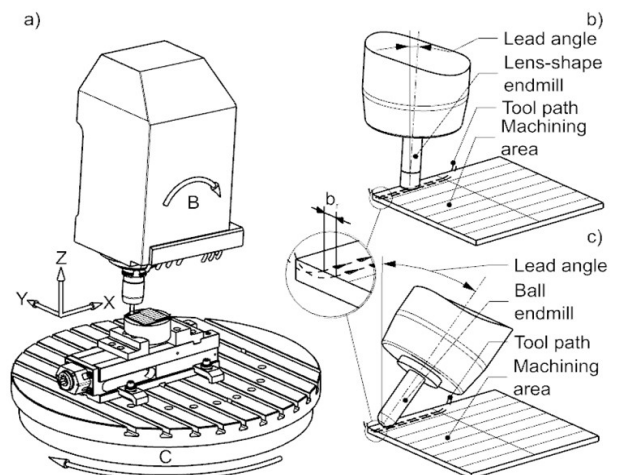
Fig. 3. Scheme of a) machine tool configuration. b) lens-shape end mill machining. c) ball end mill machining
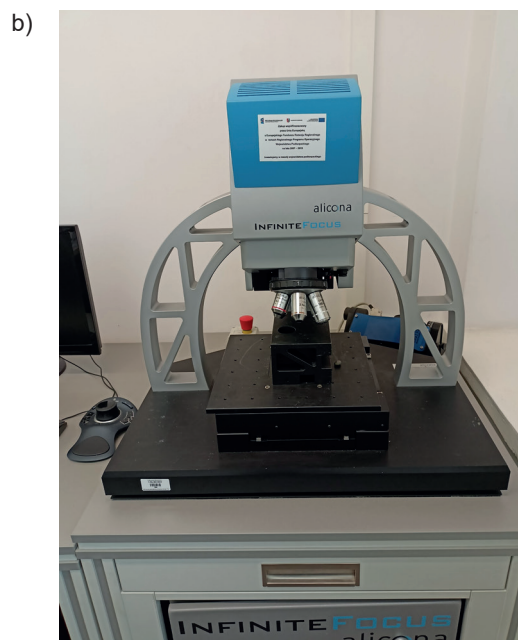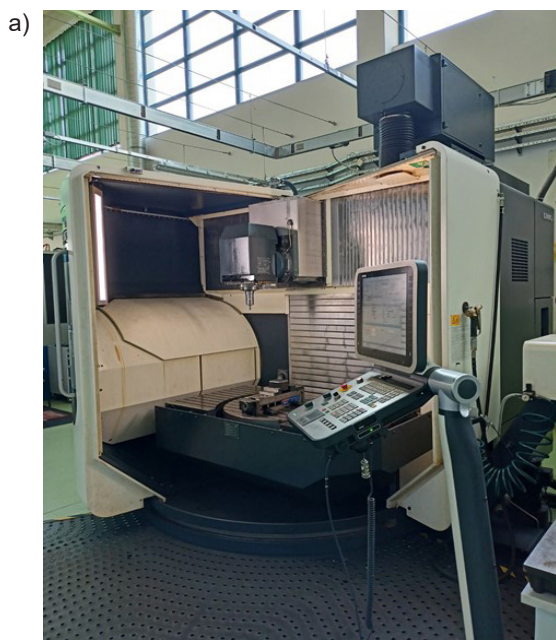
Fig. 4. Research–measurement stand: a) DMU 100 monoBLOCK milling centre. b) 3Dsystem InfiniteFocus Alicona optical micro-scope

In each operation, a lead angle was used to avoid contact of the tool tip with the machined surface. which would result in a machining at zero cutting speed. In the case of the lens-shapeend mill, the lead angle was set to 4° (Fig. 3b). Using a larger value would engage the radius r_1 in machining. On the other hand, for the ball end mill, a lead angle of 45° was set in order to achieve the maximum effective diameter of the tool (Fig. 3c). In this case, setting a larger lead angle would result in a collision of the tool holder with the workpiece. The tests were carried out on a DMU 100 monoBLOCK multi-axis milling center (Fig. 4a). The material machined during the tests was 42CrMo4 steel. The technological and kinematic parameters used during machining are presented in table 1.

The next stage of the research was focused on measurements of the machined surface topography. They were performed using the 3Dsystem Infinite Focus Alicona optical microscope (Fig. 4b).

Table 1. Technological and kinematic parameters used during the first stage of the test

No	Tool	Cutting width b_r [mm]	Cutting deapth a_p [mm]	Tool feed v_f [mm/min]	Spindle speed n [min⁻¹]	Lead angle [°]	Tilt angle [°]
1	Lens-shape end mill Emuge Franken 3544L.10020A	0.2	0.2	1145.85	7939	4	0
2		0.4					
3		0.6					
4		0.8					
5		0.2		1604.19			
6		0.4					
7		0.6					
8		0.8					
9	Ball end mill Sandvik Coromant R216.42-10030-AC19P 1620	0.2		1145.85		45	
10		0.4					
11		0.6					
12		0.8					
13		0.2		1604.19			
14		0.4					
15		0.6					
16		0.8					

Results and Discussion

For all measured surface roughness profiles. the values of the profile roughness parameters *Ra*. *Rq*. *Rz*. *Rt* (Fig. 5) show similar trends. As the path width increases linearly. The roughness parameters increase in an approximately linear manner. The change in tool feed did not significantly affect the results because the discrepancies it caused were within the measurement error margin.

a)

b)

c)

d)

Lens-shape end mill
v_f = 1145.85 [mm/min]

Lens-shape end mill
v_f = 1604.19 [mm/min]

Ball end mill
v_f = 1145.85 [mm/min]

Ball end mill
v_f = 1604.19 [mm/min]

Fig. 5. Graphs depicting profile parameters of surface roughness a) arithmetic mean deviation – *Ra*. b) Root mean square deviation – *Rq*. c) Maximum height – *Rz*. d) Total height – *Rt*

In the case of machining with a ball end mill. along with the increase in the width of the tool path. the surface roughness value increases significantly. It is particularly noticeable in the case of low path widths – when changing the b_r from 0.2 [mm] to 0.4 [mm] an increase in all roughness parameters by over 100% is visible. With a further increase in the br parameter, the increase in the roughness parameters for the subsequent steps is approximately 50% and 30%, respectively.

Measurements of the roughness of the surface milled with a lens-shape end mill show lower values compared to the surface machined with a ball end mill. For the path width b_r= 0.2 [mm], it can be observed that the values of *Ra* and *Rq* parameters constitute 30% of the values obtained for the surface machined with a ball end mill. and for *Rz* and *Rt* they equate to 50% of this value. An increase in b_r parameter causes an increase in the roughness parameters. By analysing and comparing the values of the roughness parameters, in particular for larger path widths, at least a 70% decrease in the roughness parameters values is visible.

All areal roughness parameters computed from measurement data show similar tendencies. As the path width b_r increases linearly. there is an approximately exponential increase in the surface stereometry parameters *Sa*. *Sq*. *Sz*. *St* (Fig. 6). This tendency is particularly visible on the measured surface topographies (Tab. 2). where the increase of the path width b_r is much more significant in the upper ranges of the b_r values. It is noteworthy, that for a lens-shape end mill the exponent is smaller than for a ball mill. This relationship is clearly visible on the measured topography which shows much greater differentiation for the ball mill. At higher b_r values, when comparing the analysed cutters, the results of measurements are characterized by much greater differences. For v_f= 1604.19 [mm/min] with b_r = 0.2 [mm] the
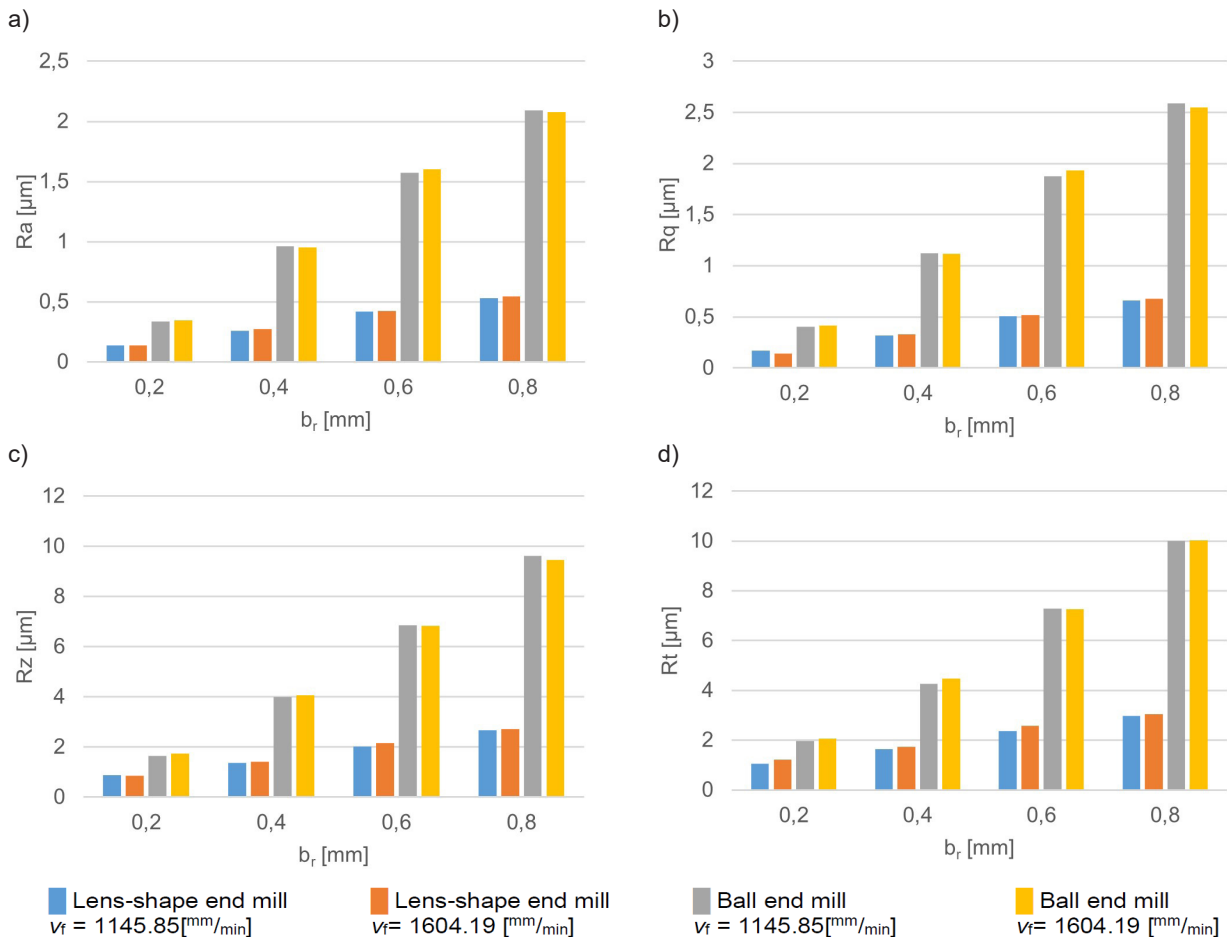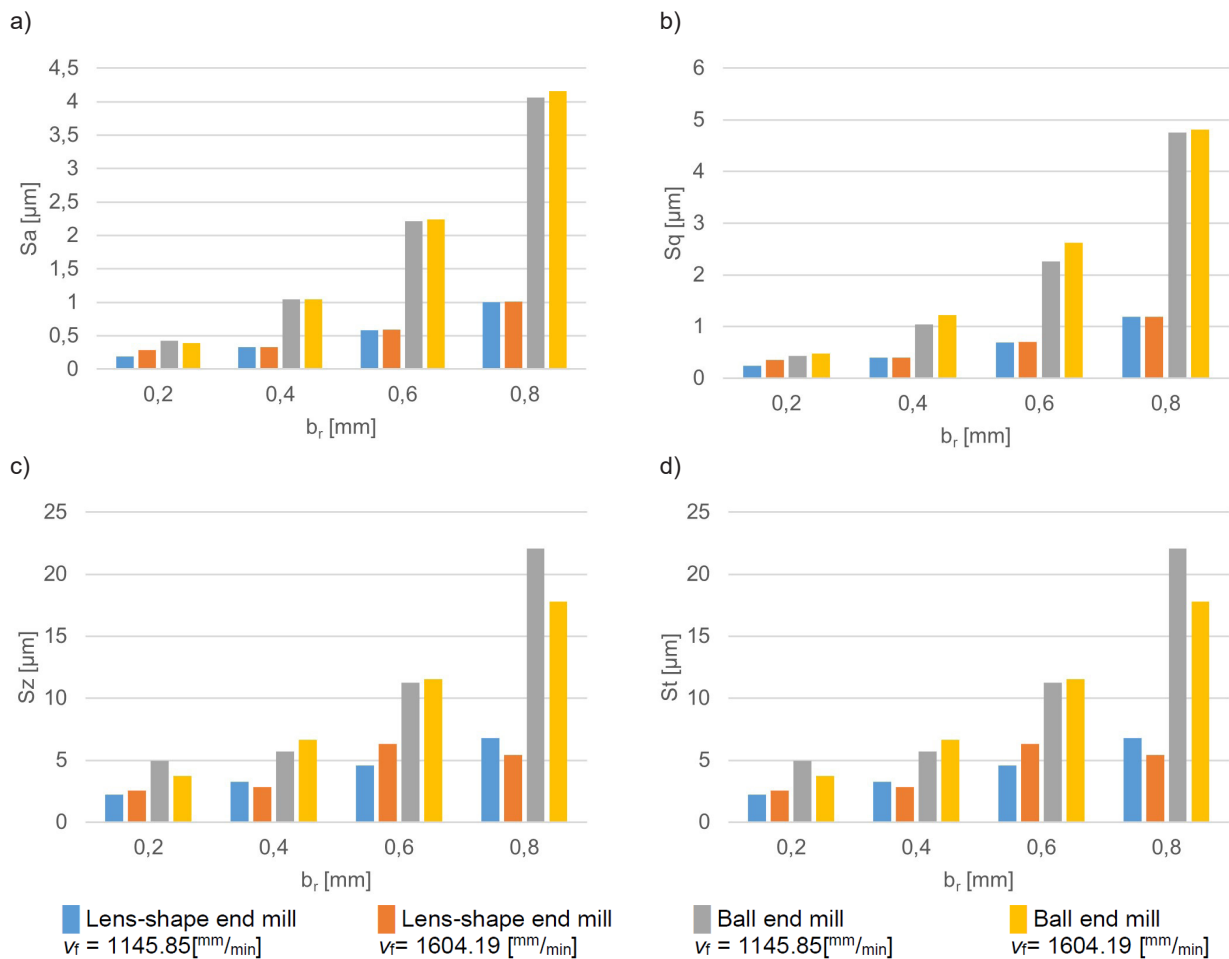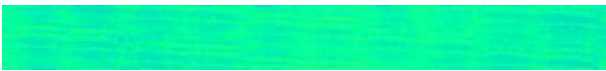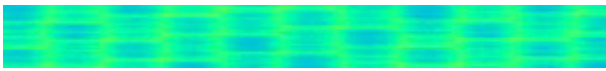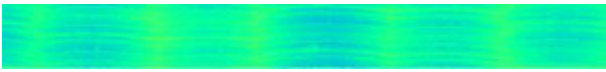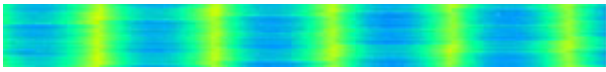
Fig. 6. Graphs depicting areal surface parameters of roughness a) arithmetic mean deviation – *Sa*. b) Root mean square deviation – *Sq*. c) Maximum height – *Sz*. d) Total height – *St*.

difference in the *Sq* parameters for both end mills is only about 0.2 [μm]. After the increase to b_r = 0.8 [mm], the measurement of the *Sq* parameter of the surface machined by the lens-shape end mill was 1.1937 [μm], and for the ball end mill it was 4.8151 [μm]. This means that for *Sq* parameter, using a lens-shape end mill with a large path width b_r, it was possible to achieve a 75% reduction of the measured value. In the case of areal surface roughness parameters, similarly to the profile rough-ness parameters, no significant changes resulting from a change in tool feed were observed. The only inaccuracy is in the measurement of the parameter *Sz* and *St*, where for b_r = 0.8 [mm] there was observed a decrease in the value of the roughness parameter with increasing tool feed. It can probably be caused by external disturbances or vibrations in the cutting process.

Table 2. Surfaces topography after milling

N° 1: v_f = 1145.85 [$^{mm}/_{min}$] b_r = 0.2 [mm] Sa = 0.19470 [μm] Sq = 0.24274 [μm]	N° 9: v_f = 1145.85 [$^{mm/min}$] b_r = 0.2 [mm] Sa = 0.42792 [μm] Sq = 0.52928 [μm]
N° 2: v_f = 1145.85 [$^{mm}/_{min}$] b_r = 0.4 [mm] Sa = 0.32818 [μm] Sq = 0.40083 [μm]	N° 10: v_f = 1145.85 [$^{mm}/_{min}$] b_r = 0.4 [mm] Sa = 1.0423 [μm] Sq = 1.2251 [μm]

N° 3: v_f = 1145.85 $[^{mm}/_{min}]$ b_r = 0.6 [mm] Sa = 0.57917 [µm] Sq = 0.68962 [µm]	N° 11: v_f = 1145.85 $[^{mm}/_{min}]$ b_r = 0.6 [mm] Sa = 2.2159 [µm] Sq = 2.5983 [µm]
N° 4: v_f = 1145.85 [mm/min] b_r = 0.8 [mm] Sa = 1.0025 [µm] Sq = 1.1867 [µm]	N° 12: v_f = 1145.85 [mm/min] b_r = 0.8 [mm] Sa = 4.0601 [µm] Sq = 4.7517 [µm]
N° 5: v_f = 1604.19 [mm/min] b_r = 0.2 [mm] Sa = 0.28247 Sq = 0.35433	N° 13: v_f = 1604.19 [mm/min] b_r = 0.2 [mm] Sa = 0.39209 [µm] Sq = 0.47982 [µm]
N° 6: v_f = 1604.19 [mm/min] b_r = 0.4 [mm] Sa = 0.33048 [µm] Sq = 0.40120 [µm]	N° 14: v_f = 1604.19 [mm/min] b_r = 0.4 [mm] Sa = 1.0463 [µm] Sq = 1.2352 [µm]
N° 7: v_f = 1604.19 [mm/min] b_r = 0.6 [mm] Sa = 0.58755 [µm] Sq = 0.70416 [µm]	N° 15: v_f = 1604.19 [mm/min] b_r = 0.6 [mm] Sa = 2.2358 [µm] Sq = 2.6240 [µm]
N° 8: v_f = 1604.19 [mm/min] b_r = 0.8 [mm] Sa = 1.0094 [µm] Sq = 1.1937 [µm]	N° 16: v_f = 1604.19 [mm/min] b_r = 0.8 [mm] Sa = 4.1592 [µm] Sq = 4.8151 [µm]

Conclusions

The results of research allow to draw the following conclusions:

- As the path width br increases, all the measured values of the surface geometrical structure parameters increase. However, the surface geometrical structure parameters increase with the path width b_r exponentially. At the same time the profile roughness parameters increase with the path width br linearly (fig. 5).
- The surfaces machined with a lens-shape mill is characterised by a lower roughness compared to the surfaces machined with ball end mill, especially when larger values of the path width b_r, even up to 75%, are considered.
- The feed in the range of values applied in the tests does not significantly affect the roughness parameters.

The research shows that the use of a lens-shape end mill allows for obtaining values of the surface topography parameters similaras the ones after the machining with a ball mill. with more than a double of the path width b_r.

The potential of using lens-shape end mills in finishing operations as an alternative to ball mills provides grounds to continue research in the same direction as for other circle segment end mills.

References

[1] Altintas. Y. Lee. P. 1998. "Mechanics and Dynamics of Ball End Milling." Journal of Manufacturing Science and Engineering. Transactions of the ASME 120 (4): 684–92.

[2] Arizmendi. M. Fernández J.. López de Lacalle L. N.. Lamikiz A. Gil A. Sánchez J. A. Campa F. J. Veiga F. 2008. „Model development for the prediction of surface topography generated by ball-end mills taking into account the tool parallel axis offset. Experimental validation." CIRP Annals - Manufacturing Technology 57 (1): 101–104.

[3] Artetxe. E. Urbikain G. Lamikiz A. López-De-Lacalle L. N.. González R. Rodal P. 2015. "A mechanistic cutting force model for new barrel end mills". Procedia Engineering 132: 553–560.

[4] Burek J. Żurek P. Żurawski K. Sułkowicz P. 2016. "Programowanie procesu 5-osiowej symultanicznej

obróbki frezem baryłkowym w aplikacji HyperMILL". Mechanik 2016/5-6: 470–471.

[5] Burek J. Żurek P. Żurawski K. 2016. "Porównanie chropowatości powierzchni złożonych po obróbce frezem baryłkowym oraz kulistym". Mechanik 2016/10: 1476–1477.

[6] Burek J. Żyłka Ł. Żurek P. Żurawski K. Sałata M. 2017. "Badania symulacyjne warstwy skrawanej frezem baryłkowym". Mechanik 2017/8-9:714–716.

[7] Burek J. Żurek P. Żurawski K. 2018 "Badania symulacyjne siły skrawania w procesie obróbki frezem baryłkowym". Mechanik 2018/10: 901–903.

[8] Engin S. Altintas Y. 1999 „Generalized modeling of milling mechanics and dynamics: Part I - helical end mills." American Society of Mechanical Engineers. Manufacturing Engineering Division 10: 345–352.

[9] Ferry W.B.S. 2008 „Virtual five-axis flank milling of jet engine impellers." The University Of British Columbia.

[10] Ferry W.B. Altintas Y. 2008 „Virtual five-axis flank milling of jet engine impellers - Part I: Mechanics of five-axis flank milling." Journal of Manufacturing Science and Engineering. Transactions of the ASME 130: 0110051–01100511.

[11] Ghorbani. M.. Movahhedy M. R. 2019. "Extraction of Surface Curvatures from Tool Path Data and Prediction of Cutting Forces in the Finish Milling of Sculptured Surfaces." Journal of Manufacturing Processes 45 (September): 273–89.

[12] Larue. A. Altintas Y. 2005. „Simulation of Flank Milling Processes." International Journal of Machine Tools and Manufacture 45 (4–5): 549–59.

[13] Ming L. Dongqing Y. Baohai W.. Dinghua Z. 2016. „Barrel cutter design and toolpath planning for high-efficiency machining of freeform surface". International Journal of Advanced ManufacturingTechnology 85 (9–12): 2495–2503.Olvera. D. E. Artetxe. M. Luo. and G. Urbikain. 2020. „5-axis milling of complex parts with barrel-shape cutter: cutting force model and experimental validation". Procedia Manufacturing 48 (2019): 528–532.

[14] Seyed Ehsan. L. K. Ismail L. 2017. „3D surface topography analysis in 5-axis ball-end milling". CIRP Annals - Man-ufacturing Technology 66 (1): 133–136.

[15] Urbikain. G. Olvera D. López de Lacalle L.N. 2016. „Stability Contour Maps with Barrel Cutters Considering the Tool Orientation." The International Journal of Advanced Manufacturing Technology 2016 89:9 89 (9): 2491–2501.

[16] Urbikain. G. Artetxe E. López de Lacalle L. N. 2017. „Numerical simulation of milling forces with barrel-shaped tools considering runout and tool inclination angles" Applied Mathematical Modelling 47: 619–636.

[17] Urbikain. G. L. N.López de Lacalle. 2018. „Modelling of surface roughness in inclined milling operations with circle-segment end mills". Simulation Modelling Practice and Theory 84: 161–176.

[18] Urbikain Pelayo. G. 2019. "Modelling of static and dynamic milling forces in inclined operations with circle-segment end mills". Precision Engineering 56 (3): 123–135.

[19] Urbikain Pelayo. G. Olvera-Trejo D. Luo M. López-De-Lacalle L. N. Elías-Zuniga A. 2021. „Surface roughness prediction with new barrel-shape mill considering runout: Modeling and validation". Measurement 173: 1–10.

[20] Wang. D. Wu Yi C. Tian L. Ru Feng X. 2009. „Five-axis flank milling of sculptured surface with barrel cutters". Key Engineering Materials 407–408 (2): 292–297.

[21] Wojciechowski S. 2014 „Siły w procesie skrawania frezem kulistym zahartowanej stali" Politechnika Poznańska. Wydział Budowy Maszyn i Zarządzania. Poznań.

[22] YaoAn. L. QingZhen B. BaoRui D. ShuLin C.. LiMin Z. Kai H. 2014. „Five-axis strip machining with barrel cutter based on tolerance constraint for sculptured surfaces" International Journal of Mechanical Aerospace. Industrial Mecatronic and Manufacturing Engineering 8 (10): 1779–1784.

[23] EMUGE Corp. „Circle Segment Cutters." https://www.emuge.com/sites/default/files/literature/Circle-Segment-Turbine-Catalog-2020.pdf (2021.07)

[24] Hoffman Group. „Dynamic 5-axis milling with GARANT PPC mills and PPC indexable inserts." https://www.hoffmann-group.com/US/en/hus/ areas-of-application/machining/solid-carbide-barrel-milling-cutter-garant-ppc/e/68093/. (2021.07).

mgr inż. Piotr Żurek
Rzeszow University of Technology,Faculty of Mechanical Engineering and Aeronautics,Department of Manufacturing Techniques and Automation
ul. Wincentego. Pola 2 35-959 Rzeszów, Poland
e-mail: p_zurek@prz.edu.pl

mgr inż. Karol Żurawski
Rzeszow University of Technology, Faculty of Mechanical Engineering and Aeronautics, Department of Manufacturing Techniques and Automation
ul. Wincentego. Pola 2 35-959 Rzeszów, Poland
e-mail: zurawski@prz.edu.pl

mgr inż. Artur Szajna
Rzeszow University of Technology, Faculty of Mechanical Engineering and Aeronautics, Department of Manufacturing Techniques and Automation
ul. Wincentego. Pola 2 35-959 Rzeszów, Poland
e-mail: a.szajna@prz.edu.pl

mgr inż. Rafał Flejszar
Rzeszow University of Technology, Faculty of Mechanical Engineering and Aeronautics, Department of Manufacturing Techniques and Automation
ul. Wincentego. Pola 2 35-959 Rzeszów, Poland
e-mail: r.flejszar@prz.edu.pl

mgr inż. Marcin Sałata
Rzeszow University of Technology, Faculty of Mechanical Engineering and Aeronautics, Department of Manufacturing Techniques and Automation
ul. Wincentego. Pola 2 35-959 Rzeszów, Poland
e-mail: msalata@prz.edu.pl

Like us on Facebook
www.facebook.com/sigmanot

Follow us on Instagram
www.instagram.com/sigmanot

WYDAWNICTWO SIGMA-NOT

NUMERICAL SIMULATION OF FLOW THROUGH MICROCHANNELS OF TECHNICAL EQUIPMENT WITH TRIANGULAR AND RECTANGULAR ELEMENTS OF ROUGHNESS

Małgorzata KMIOTEK   ORCID: 0000-0003-3229-0367
Tomasz IWAN

A b s t r a c t: This paper presents a computational study on an influence of a rough surface on the fluid flow in a microchannel used in various technical microdevices of complex products. Two-dimensional axially symmetrical microchannels with a circular cross-section were considered. The fluid flow were simulated as simple geometric figures, i.e. a triangle and a rectangle with different height h and different distance s between each other. The flow equations were solved with Ansys / Fluent software. A streamline analysis is performed to investigate the flows in the recirculation zone behind the roughness elements. It was found that the friction factor increases with increasing height of rough elements. The coefficient of friction factor is greater for rectangular elements than for triangular elements, and decreases as the geometry of the element changes. Friction factor decreases as the Reynolds number increases. The authors indicate that in the production of microchannels of complex products, it is recommended to use triangular elements to model roughness.

K e y w o r d s: natural mechanical engineering, roughness, microchannels, Ansys, friction factor

S t r e s z c z e n i e: Celem pracy jest określenie wpływu chropowatej powierzchni na przepływ płynu w mikrokanałach stosowanych w różnych mikrourządzeniach technicznych złożonych wyrobów. Rozpatrywano dwuwymiarowy osiowo-symetryczne mikrokanały o przekroju kołowym. Chropowatość została zasymulowana jako proste figury geometryczne tj. trójkąt i prostokąt o różnej wysokości *h* i różnej odległości s między sobą. Równania przepływowe zostały rozwiązane za pomocą oprogramowania Ansys/Fluent. Przeprowadzana jest analiza linii prądu w celu zbadania przepływów w strefie recyrkulacji za elementami chropowatości. Stwierdzono, że współczynnik tarcia wzrasta wraz ze wzrostem wysokości elementów chropowatych. Współczynnik tarcia jest większy dla elementów prostokątnych niż trójkątnych i zmniejsza się wraz ze zmianą geometrii elementu. Straty tarcia maleją wraz ze wzrostem liczby Reynoldsa. Autorzy wskazują, że w produkcji mikrokanałów złożonych wyrobów do modelowania chropowatości zaleca się używać elementów trójkątnych.

S ł o w a k l u c z o w e: inżynieria mechaniczna, chropowatość, mikrokanały, Ansys, straty tarcia

Introduction

The miniaturization of devices, especially electronic devices, resulted in the miniaturization of mechanical parts and machines, which allowed for the development of production processes for very small machines, e.g. microengines, micropumps, and microreactors. Micro-components and microdevices are increasingly used in many industries: from energy generation, fuel cells to bio-medical devices, as well as cooling systems. Due to the intensive development of more complex systems in small scales, microchannels have become an inseparable part of most microfluidic devices, hence the necessity to use small cross-sections, therefore the requirements and requests related to the use of mini and microchannels are increasing. The flow and heat transfer models developed and tested for macrochannels do not take into account the significant phenomena in the microchannels, and the difference increases with the reduction of the dimension characterizing the flow and the surface treatment method. As the channel size decreases, the effect of roughness on fluid flow also increases. A surface roughness is a set of irregularities, i.e. peaks and pits on the real surface of an object with relatively small intervals between the vertices [2, 4, 8].

At the macro scale, the material from which the element was made, the type of processing and processing parameters undoubtedly have the greatest influence of the surface roughness. The surface can most often be characterized as a combination of two profiles – waviness and roughness (some surfaces also show a shape error). Surface roughness is the result of the simultaneous interaction of many independent factors, both random and determined, and as a result it has a very complex microgeometry. The roughness is influenced by many factors, such as: decohesion processes, plastic deformation in the cutting zone and the formation of chip segments, friction of the tool contact surface against the machined surface, metal crystalline structure, chip friction against the machined surface, etc. [2, 8].

During the surface treatment of the micro-scale surface roughness is unavoidable. There are many types

of micromachining methods, such as EDM (electrical discharge machining), ECM (electrochemical machining), etching, micro-milling, and so on; the precision of processing of these methods ranges from 10^{-2} µm to 5 µm. Depending on the manufacturing process channels they may, however, even have a surface roughness comparable to the dimensions of the channel. To properly design a microdevice, it is necessary to establish the physical laws that govern fluid flow and heat transfer in micro--geometry to taking into account performance of the microdevice, thus it involves identification of the surface of microchannels [4].

Although the flows in rough macrochannels are very well known, the micro scale has not been fully researched yet. Therefore, in the last few decades, many experimental studies have been conducted on the microchannels of different hydraulic diameter. Some studies show that there are no significant differences in the time of transition from laminar to turbulent flow, and no differences in the flow between the macro and micro scale. In contrast, other studies indicate a change in the character of flow below the critical value of the Reynolds number (2300) and a higher coefficient of roughness that occurs in channels with small hydraulic diameter. It is suggested by the increase of the roughness effect together with the decrease of the channel size [1, 9].

At the microscale level, it is impossible to obtain a completely smooth wall surface. According to the knowledge of macrosystems, when the relative roughness is less than 5%, its influence on the coefficient of friction is negligible [4].

For microscale channels, experimental and numerical results showed that surface roughness has a significant effect on heat transfer and heat transfer. For example, the experiment of Kandlikar et al. indicated that for a 0.62 mm pipe with a relative roughness height of 0.355%, the influence of roughness on the friction factor and heat transfer was significant [3].

A very extensive literature study is shown in [2]. The main goal was to investigate the effect of roughness on the friction coefficient and the critical Reynolds number. The study was based on 33 scientific articles (a total of 5569 data were collected) for flows in micro- and mini-channels with different wall roughness. The authors concluded that if the relative roughness height is <1%, it has little effect on the friction coefficient and the critical Reynolds number. The value of 1% is suggested as a threshold to distinguish smooth and rough micro- and mini-channels. However, it is not easy to obtain a perfectly smooth surface using this criterion in real applications [1].

However, while a large pool of experimental data is available, there is not yet a complete understanding of all aspects of microscale flow behaviour, therefore numerical methods are used to model flows at this scale. The computational approach can therefore be useful for understanding the basic physics of the problem on a microscale, because it is possible to analyze several aspects difficult to grasp in an experiment at the same time, but also indicate the direction of surface technology in microdevices and microchannels.

Most often in the literature, the surface roughness is modeled with simple geometric shapes, e.g. triangles, rectangles, squares, ellipses, trapeziums [6, 9]. In the paper [6], the authors simulate the flow in microchannels, where the roughness is modeled, inter alia, by means of triangles and rectangles. The tested relative roughness ranged from 2.5 to 15%. The analysis shows that the roughness influences on the streamline distribution. This increases the friction and the pressure differences between the inlet and outlet. With a high roughness value, this can keep the flow breaking off near the wall and the formation of recirculation zones. The detachment and recirculation flow is probably the main cause of increased friction and pressure drop [9].

Research methodology

The aim of the study is an estimation of the effect of roughness on the laminar flow of fluid in microchannels, as well as to select an appropriate method of roughness modelling (so that it best reflects the actual phenomenon) and to compare it with the literature.

Two-dimensional axially symmetric micro channels with a circular cross-section were considered. Elements of the rectangular or triangular shape are placed on the
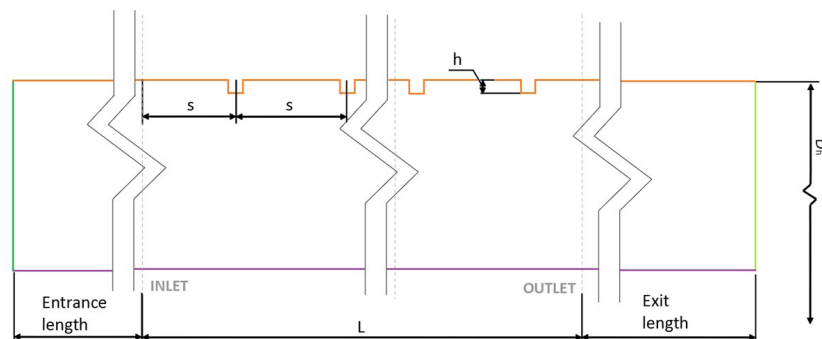

Fig. 1. The geometry of the microchannel

walls (simulating the roughness of the channel). Elements simulating roughness with a constant width w and different heights h are placed in different distances s. The microchannel geometry is shown in Fig. 1.

The flow was assumed to be two-dimensional, axisymmetric, incompressible and steady (the influence of gravity is neglect). A characteristic dimension of the Reynolds number is the diameter of the channel. The working medium is water (fluid density $\rho = 998 \frac{kg}{m^3}$, dynamic viscosity $\mu = 0{,}001\ Pa \cdot s$).

The parameters used in the calculations are presented in Table 1, and the dimensionless parameter values are presented in Table 2.

Table 1. Parameters used for calculations

Characteristic	Symbol	Value	Unit
microchannel length	L	1	mm
microchannel diameter	D_h	50	µm
element height	h	1/1,75/2,5	µm
element width	w	2	µm
distance between elements	s	10/15/20	µm
inlet velocity	V_{in}	2,01 – 42,12	m/s

Table 2. Dimensionless height and distance between roughness elements

h	h/D_h	s	s/D_h
1	0,02	10	0,2
1,75	0,035	15	0,3
2,5	0,05	20	0,4

The flow realized in the micro channel results from the principles of conservation of mass and , momentum [4]:

1. The conservation of mass:

$$\frac{\partial \rho}{\partial t} + \operatorname{div}(\rho \bar{V}) = 0 \qquad (1)$$

2. The conservation of momentum:

$$\rho \frac{\partial \overline{V}}{\partial t} = \rho \bar{F} - \operatorname{grad}\ p + \mu \Delta \bar{V} \qquad (2)$$

where: $\bar{V}\left[\frac{m}{s}\right]$ – velocity vector, $\rho\left[\frac{kg}{m^3}\right]$ – fluid density, $\bar{F}\ [N]$ – vector of mass forces, $P\ [Pa]$ – fluid pressure.

The system of equations adopted for modelling can be written in the form of equations [4]:

• Equations of continuity:

$$\frac{1}{r}\frac{\partial (r u_r)}{\partial r} + \frac{\partial (u_z)}{\partial z} = 0 \qquad (3)$$

• Momentum equations (Navier - Stokes):

$$\rho\left(V_r \frac{\partial V_r}{\partial r} + V_z \frac{\partial V_r}{\partial z}\right) = -\frac{\partial p}{\partial r} + \mu\left[\frac{1}{r}\frac{\partial}{\partial r}\left(r\frac{\partial V_r}{\partial r}\right) - \frac{V_r}{r^2} + \frac{\partial^2 V_r}{\partial z^2}\right]$$

$$\rho\left(V_r \frac{\partial V_z}{\partial r} + V_z \frac{\partial V_z}{\partial z}\right) = -\frac{\partial p}{\partial z} + \mu\left[\frac{1}{r}\frac{\partial}{\partial r}\left(r\frac{\partial V_z}{\partial r}\right) + \frac{\partial^2 V_z}{\partial z^2}\right] \qquad (4)$$

The commercial ANSYS software was used to solve the equations – the Fluent module, using the finite volume method. The boundary conditions adopted for the analysis are:
• at the inlet to the channel outlet profile established reference pressure (Pout = 0 Pa),
• zero tangential velocity on the channel walls (also impenetrability of the walls),
• axial symmetry.

When determining the type of flow, a dimensionless similarity number is defined - the Reynolds number given by the formula [4]:

$$Re = \frac{\rho V D_L}{\mu} \qquad 5)$$

where: $D_L\ [m]$ – characteristic dimension, $\mu\left[\frac{kg}{m \cdot s}\right]$ – dynamic viscosity, $V\left[\frac{m}{s}\right]$ – flow velocity

To determine the effect of roughness on the flow in the microchannel, the formulas used in macrochannels and milichannels are used, and the dimensionless coefficient of friction (Fanning or Dracy) can be used to determine the pressure drop [3]. The Fanning friction coefficient (f_F) is defined as:

$$f_F = \frac{\tau_w}{\frac{1}{2}\rho u_m^2} \qquad (6)$$

where: $\tau_w\ [Pa]$ – shear stresses, $u_m\left[\frac{m}{s}\right]$ – average velocity in the channel.

The Dracy coefficient of friction (f_D), related to the Fanning coefficient of friction, is expressed as:

$$f_D = 4f_F \qquad (7)$$

The Dracy coefficient is also defined as the ratio of the Poiseuille number P_o to the number R_e as in the formula [6]:

$$f_D = \frac{P_o}{R_e} \qquad (8)$$

The Poiseuille number assumes a constant value, in the case of developed laminar flow it differs depending on the shape of the channel cross-section. For the channel

with a circular cross-section, the Poiseuille number is assumed to be constant at 64.

Formula for pressure drop taking into account frictional losses:

$$\Delta p = \frac{2 f_D \rho u_m^2 L}{D} \qquad (9)$$

where: $D\,[m]$ – microchannel diameter or hydraulic diameter if the channel cross-section is other than circular, $L\,[m]$ – channel length.

The Dracy coefficient of friction depends on: the type of flow, wall roughness, channel geometry (length, diameter) and is most often determined using the Moody diagram. The Dracy coefficient of friction for laminar flow is based on the Hagen-Poiseuille law [3]:

$$f_D = \frac{64}{Re} \qquad (10)$$

In macro and microscale in laminar flow, the friction loss coefficient depends on the Reynolds number and not on the roughness [3].

In the construction of the microchannel geometry an entrance length was included. The entrance length was calculated from the formula [4]:

$$h/D \cong 0{,}05\,Re \qquad (11)$$

The value of the entrance length was adopted at 6 mm for R_e = 2100. The value of the exit length was set at 0.5 mm.

To investigate the effect of mesh density on the results, 4 types of mesh were generated (Fig. 2) for the same Reynolds number (R_e = 1100; h = 1.75 µm; s = 15 µm). When comparing the results, the Grid Convergence Index (GCI) was used, related to the average velocity in the cross-section located in the middle of the canal length [5]:

$$CGI = F_s * \frac{\left| \frac{u_{h2} - u_{h1}}{u_{h1}} \right|}{a^p - 1} * 100 \qquad (12)$$

where: $F_s\,[-]$ – safety factor, $u_{h1}, u_{h2}\,\left[\frac{m}{s}\right]$ – selected parameter (velocity was assumed in the middle of the channel length, 12.5 µm from the axis of symmetry $h_1, h_2\,[-]$ – number of finite elements, $p = \frac{h_2}{h_1}\,[-]$ – mesh compaction factor, $a\,[-]$ – calculation approximation order (assumed value is 2).

| Number of elements: 28169 Size: 0,75 µm | Number of elements: 63229 Size: 0,5 µm | Number of elements: 304679 Size: 0,1 µm | Number of elements: 424632 Size: 0,025 µm |
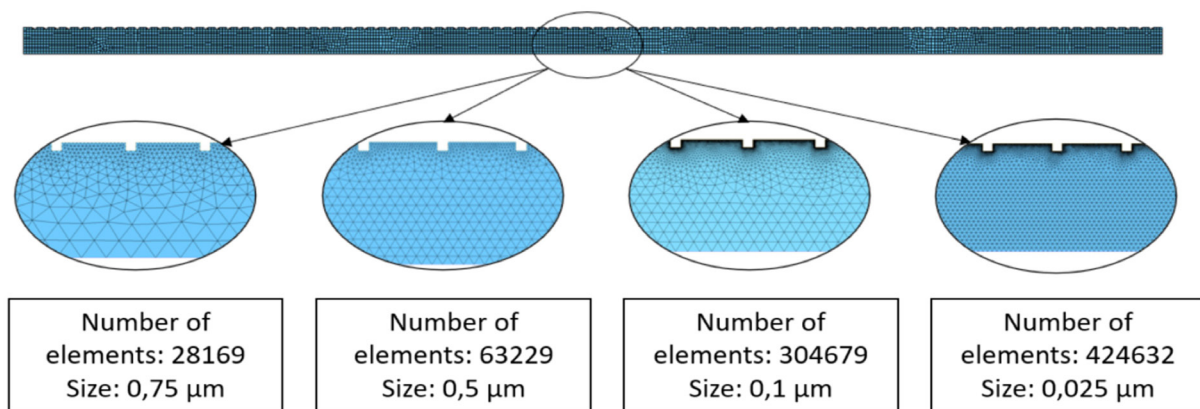
Fig. 2. The grids used to check the recommended length of the element

To optimize the mesh, a study of the GCI coefficient was performed. These studies have indicated, the GCI coefficient is less than 0.4% with an element size of 0.1 µm.

Results

To investigate the influence of roughness on the flow in the microchannel, calculations of the flow system were performed. The changes were analysed:

1) the shape of the roughness element - rectangle or triangle,
2) the height of the roughness element h in relation to the diameter of the microchannel D – parameter h/D,
3) the distance between the roughness elements s in relation to the diameter of the microchannel D – parameter s/D,
4) Reynolds number (flow velocity), where R_e = 100-2100.

The influence of the shape (rectangle, triangle) and height of the roughness element, i.e. the value of the

Fig. 3. Distribution of the streamline in the microchannel when s/D = 0.3 with triangular roughness elements   a) h/D =0.02; b) h/D = 0.035; c) h/D =0.05

h/D parameter, on the flow in the microchannel was investigated, and on the basis of the obtained numerical results, stream lines were drawn, which was shown in Figs. 3 and 4. The parameter describing the change in the height of the roughness element is h/D, with the following values were analyzed h/D = 0.02; b) h/D = 0.035; c) h/D = 0.05; with constant parameter s/D = 0.3. The flow was carried out at the velocity of V = 2.01 m/s, which corresponds to the number R_e = 100. The results of flows in microchannels with roughness in the form of triangular and rectangular elements are presented in Figs. 3 and 4. The deformation of the flow image was shown. The analysis of the test results shows the formation of circulation zones behind the elements (in some cases, circulation also occurs before the element). The flow was not disturbed only in the case of triangular elements with h/D = 0.02. On the basis of the analysis of the length of the vortices, it can be concluded that the height of the

element is the main parameter determining the length of the vortex. For h/D = 0.035 and h/D = 0.05, of the vortex length increases by 140% and 393.3%, respectively, against h/D = 0.02. The second parameter is the element type – rectangular elements disturb the flow more.

The distance between the roughness elements, i.e. the influence of the parameter s/D was investigated. It was observed that for the height of the triangular element, when h/D = 0.02, there is no vortex zone, and for rectangular elements, increasing the distance does not change the length of the vortex or the length of the vortex is slightly colder. In other cases, when the vortices do not interact, a slight decrease in the length of the vortex, on average 2.85% for rectangular elements, 1.13% for triangular elements, is noticeable, so the influence of the spacing of the roughness elements is marginal.

In order to compare the friction factor calculated on the basis of numerical simulations in microchannels with
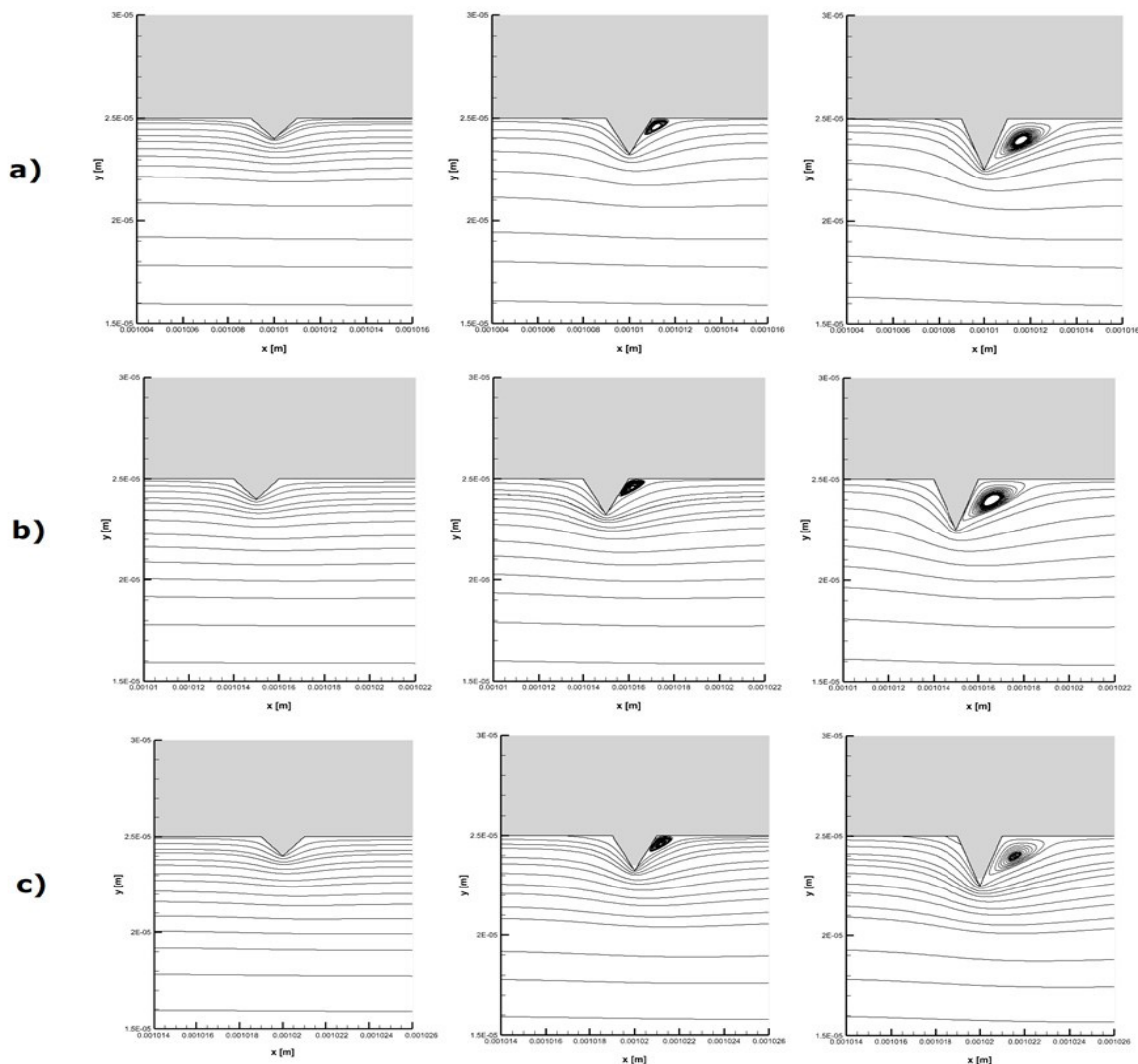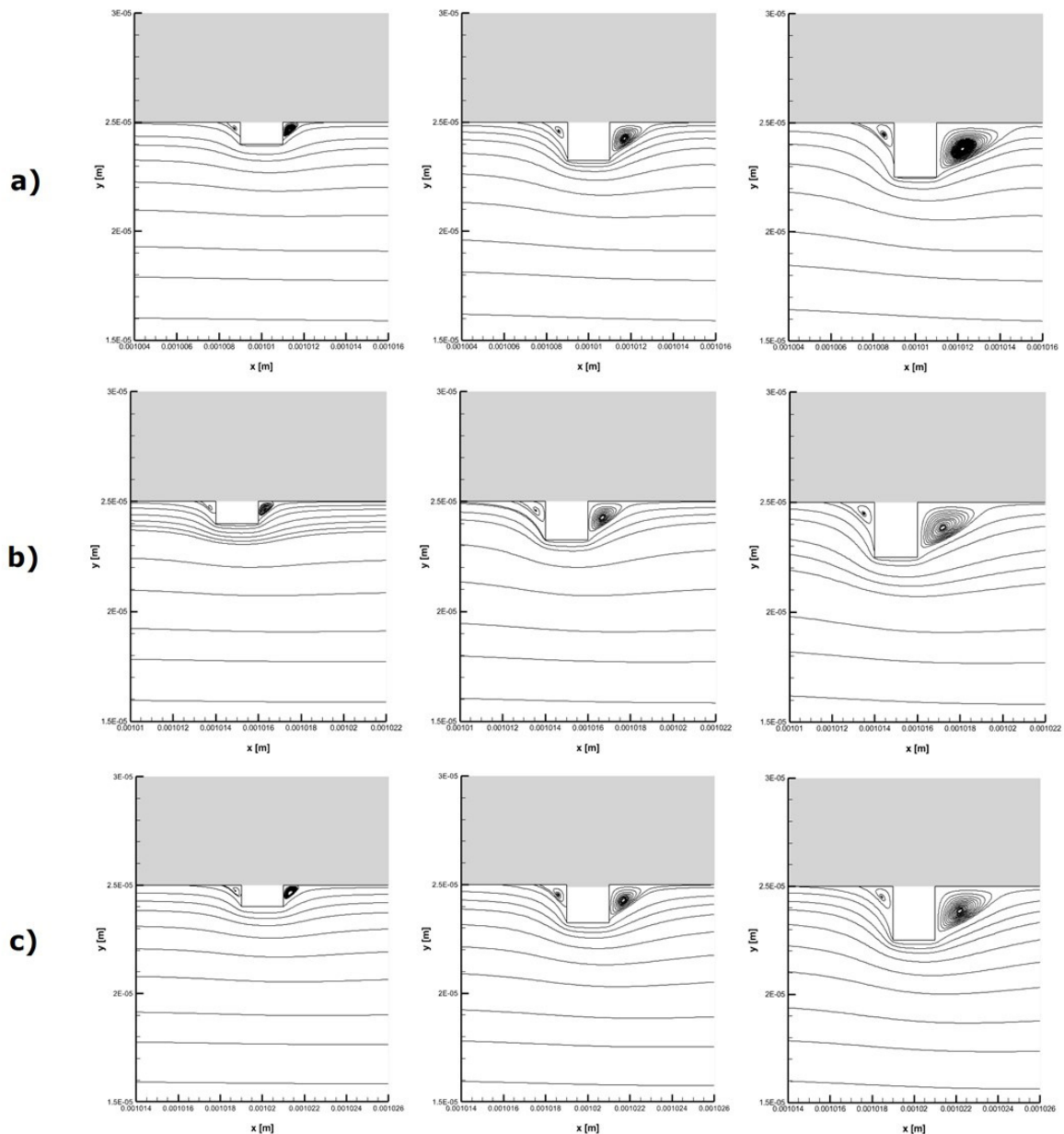
Fig. 4. Distribution of the streamline in the microchannel when *s/D* = 0.3 with rectangular roughness elements a) *h/D* =0,02; b) *h/D* = 0,035; c) *h/D* =0,05

the roughness simulated with simple geometric elements in the form of triangles and rectangles. The calculation results are presented in Fig. 5 and compared with the results resulting from the Hagen-Poiseuille law (formula 10).

The results obtained from the simulation presented in Fig. 5 show that the value of the friction factor increases with the increase of the roughness height. This is a characteristic trend for both the model with triangular and rectangular elements. There is also a reduction in the coefficient as the distance between the elements simulating roughness increases (for both cases). Rectangular obstacles have a much higher friction factor than triangular obstacles (5% higher on average). The greater

the roughness, the greater the difference between rectangular elements compared to triangular elements. The obtained values of the coefficients on the basis of calculations are higher than in the case of the friction factor obtained by analytical calculations, both for rough elements modelled by means of triangles and rectangles. Rough triangular elements have a smaller discrepancy between the friction factor and the literature data (maximum discrepancy of 21% for triangular elements compared to 30% for rectangular obstacles).

In order to investigate the effect of the Reynolds number on of the friction factor value, a comparison was made of the flows in rough microchannels with triangular, rectangular elements, when *s/D* = 0.4 (selected on
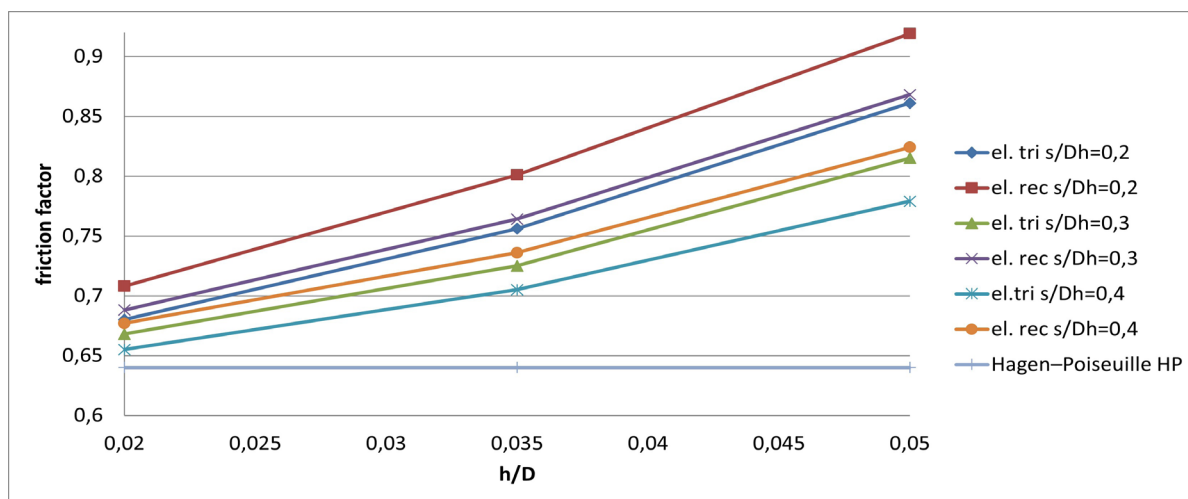
Fig. 5. Comparison of the friction factor values calculated on the basis of the simulation and the Hagen-Poiseuille law
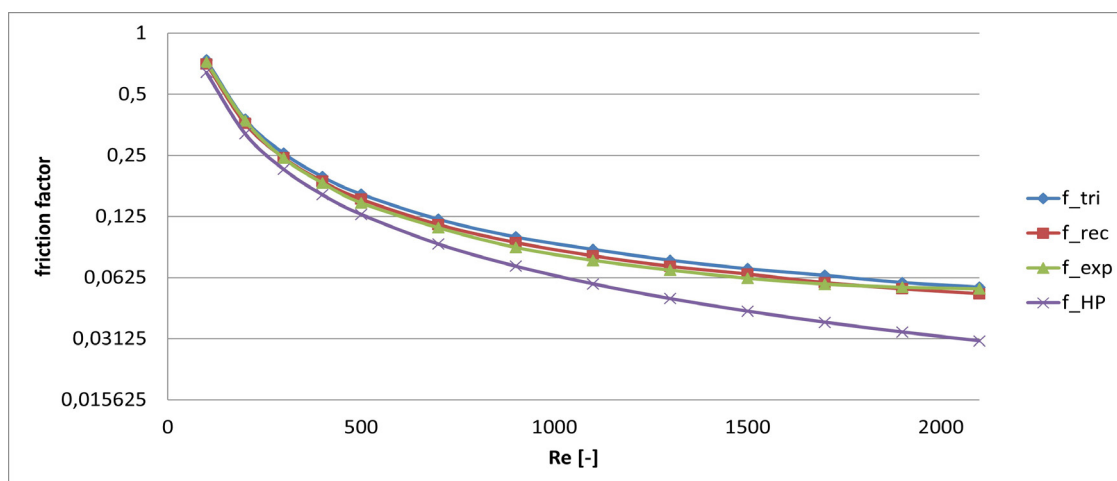
Fig. 6. Comparison of the friction factor values calculated on the basis of the simulation, experimental data [7] and the Hagen-Poiseuille law

the basis of the previous analysis), *h/D* = 0.035 and the experimental data contained in [7] for a microchannel with a diameter of 50 μm and a roughness measured at the level of 1.75 μm, which corresponds to *h/D* = 0.035, and the results were compared to the Hagen-Poiseuille law (Fig. 6).

The results show that the friction factor decreases as the Reynolds number increases. The greatest discrepancies with the experimental data occur for the Re numbers in the range 500-1150. For rectangular elements, all relative differences in this range exceed 10%. On the other hand, triangular elements generate 3.9-5.8% of the relative error in the given range. Triangular elements simulate the real surface condition much better.

Conclusion

Along with the development of miniaturized technologies, microchannels have found wide application in cooling systems of various technical devices, especially electronic devices. However, the flow behaviour in rough microchannels still needs to be investigated. In the article, the influence of roughness modelled with triangular and rectangular elements on the flow and friction factor in microchannels was examined numerically. The analysis of the numerical obtained results showed a significant influence of the roughness on the flow in the microchannel. The conclusions based on the results are as follows:

- The main mechanism to influence fluid flow is the creation of recirculation zones downstream of the roughness elements.
- The length of the recirculation zones increases with the height of the rectangular and triangular elements.
- The main parameters affecting the length of the recirculation zones are the roughness height as well as the element type - this effect is less visible for the triangular elements with the smallest height.
- The higher the roughness height, the greater the pressure difference between rectangular elements in relation to triangular elements.
- As the roughness of rectangular and triangular elements increases, the value of the pressure loss coefficient increases.
- There is also a reduction in the loss factor as the distance between the roughness simulators increases (for both cases).
- The friction factor decreases as the Reynolds number increases (for both).
- Triangular elements achieve a much lower friction factor than rectangular elements.

In the production of microchannels of complex products taking into account roughness, it is recommended to use triangular elements for modelling it as a simple figure - they show greater convergence with experimental and literature data.

References

[1] Dai Baomin; Li Minxia & Ma, Yitai. 2014. „Effect of surface roughness on liquid friction and transition characteristics in micro- and mini-channels". Applied Thermal Engineering 67 (1–2): 283–293. doi:10.1016/j.applthermaleng.2014.03.028.

[2] Datta Aparesh et al. 2019. „A review of liquid flow and heat transfer in microchannels with emphasis to electronic cooling". Sādhanā 44 (12) (abenduak 15): 234. doi:10.1007/s12046-019-1201-2. http://link.springer.com/10.1007/s12046-019-1201-2.

[3] Kandlikar S. G. 2005. „Roughness effects at microscale - Reassessing Nikuradse's experiments on liquid flow in rough tubes". Bulletin of the Polish Academy of Sciences: Technical Sciences 53 (4): 343–349.

[4] Kandlikar S. G., Dongqing Li, Stéphane Colin, Srinivas S. Garimella and M. King. 2006.. Heat Transfer and Fluid Flow in Minichannels and Microchannels. Elsevier.. doi:10.1016/B978-0-08-044527-4.X5000-2.

[5] Kmiotek M. & Kucaba-Piętal, A. 2018. „Influence of slim obstacle geometry on the flow and heat transfer in microchannels". Bulletin of the Polish Academy of Sciences: Technical Sciences 66 (2): 111–118. doi:10.24425/119064.

[6] Lalegani Fakhrodin et al. 2018. „Effects of different roughness elements on friction and pressure drop of laminar flow in microchannels". International Journal of Numerical Methods for Heat & Fluid Flow 28 (7) (uztailak): 1664–1683. doi:10.1108/HFF-04-2017-0140.

[7] Mohiuddin Mala, Gh. & Li, Dongqing. 1999. „Flow characteristics of water in microtubes". International Journal of Heat and Fluid Flow 20 (2) (apirilak): 142–148. doi:10.1016/S0142-727X(98)10043-7.

[8] Whitehouse, David. 2004. Surfaces and their Measurement. Butterworth-Heinemann.

[9] Zhang, Chengbin; Chen, Yongping & Shi, Mingheng. 2010. „Effects of roughness elements on laminar flow and heat transfer in microchannels". Chemical Engineering and Processing: Process Intensification 49 (11) (azaroak): 1188–1192. doi:10.1016/j.cep.2010.08.022.

dr inż. Małgorzata Kmiotek
Department of Aerospace Engineering
Faculty of Mechanical Engineering and Aeronautics
Rzeszow University of Technology
e-mail: kmimal@prz.edu.pl

mgr inż. Tomasz Iwan
Graduate Faculty of Mechanical Engineering and Aeronautics
Rzeszow University of Technology

Stanisław KOZIOŁ   ORCID: 0000-0001-5773-8098
Tomasz SAMBORSKI   ORCID: 0000-0001-6914-1678
Mariusz SICZEK   ORCID: 0000-0002-9060-7994
Andrzej ZBROWSKI   ORCID: 0000-0002-6146-3522

A b s t r a c t: The article presents the method and a prototype system to verify the degree of protection against dust penetration developed in accordance with the PN-EN-60529:2003 standard requirements. The solution in question enables the performance of normative tests with reference to the degrees of protection provided by enclosures (IP code) as well as extended tests concerning the evaluation of operational reliability of devices exposed to dust. The authors present the test method, the architecture of the developed system, and the prototype verification tests.

K e y w o r d s: Dustiness, IP code, protection against dustiness, dust-tightness, verification test

S t r e s z c z e n i e: W artykule przedstawiono metodę i prototypowy system badania odporności na statyczne oddziaływanie pyłów, opracowany na podstawie wymagań normy PN-EN 60529:2003. Przedstawione rozwiązanie umożliwia realizację badań normatywnych w odniesieniu do stopnia ochrony IP zapewnianych przez obudowy, a także w zakresie rozszerzonym do oceny niezawodności działania urządzenia poddanego oddziaływaniu pyłu. Zaprezentowano opis metody, strukturę opracowanego systemu i badania weryfikacyjne prototypu.

S ł o w a   k l u c z o w e: zapylenie, kod IP, ochrona przed zapyleniem, pyłoszczelność, badania testowe

Introduction

The Łukasiewicz Research Network – Institute for Sustainable Technologies is the third biggest research network in Europe. It delivers attractive, comprehensive and competitive technological solutions, also those tailored to the needs of and requested by companies as part of the "challenge us" campaign – a company's request is analysed by a group of 4,500 scientists within no more than 15 business days and an effective solution that is ready to implement is proposed. In doing so, Łukasiewicz Network, at no extra cost to be incurred by a company, engages recognised and highly-qualified researchers and unique scientific equipment, which enables the network to meet companies' needs and expectations. A business owner may choose to contact the network via an on-line form available on https://lukasiewicz.gov.pl/en/for-business/, or visit one of its affiliated institutes or branches in more than 50 locations across Poland, and they may be sure that they will always be provided with the same high-quality product or service, no matter which entity they contact. Łukasiewicz's Network scientific potential is concentrated in the following research areas: Health, Smart Mobility, Digital Transformation, and Sustainable Economy and Energy. The innovative system to monitor the safety of operation of technical devices working in a dust-filled environment, developed at the Łukasiewicz Research Network – Institute for Sustainable

Technologies and described in this article, is an example of a solution proposed in response to a "challenge us" request made in the Health and Energy areas.

The device enclosure provides the user with protection against access to live or moving mechanical parts of the device, the contact with which may be hazardous in different operating conditions [2, 12]. The enclosure also constitutes basic protection against external influences or conditions, such as dustiness, electromagnetic radiation, moisture, water, etc. Such influences or conditions may increase the risk of electrocution, explosion, deterioration of operating parameters or a device failure. Particularly stringent requirements as regards dust tightness apply to armament systems [6, 7], fire protection systems [10, 9], aviation systems [8], and mining systems [1].

Tests to verify dust tightness of device enclosures are carried out in order to define the degree of protection against dust penetration or to evaluate the operational reliability of a device exposed to dust (e.g. transported or operated in a dust-filled environment).

One of the methods to define the degree of protection provided by enclosures is discussed in the PN-EN 60529:2003 standard [5]. The identification code contains the IP code and two characteristic numerals and two additional letters (non-obligatory) that define additional requirements or provide additional information about the enclosure. First characteristic numerals (0–6) refer to the following two acceptance conditions:

- the degrees of protection against access to hazardous parts by preventing or limiting the ingress of a part of the human body or an object held by a person; and
- the degrees of protection against the penetration of solid foreign objects (including dust). As regards special manufacturing, additional requirements defined in separate standards apply [4].

Method description

The method for testing the degree of protection against dust penetration provided by a device enclosure is defined and regulated by normative requirements (Fig. 1). Tests need to be carried out with the use of an advance test device composed of pneumatic, mechanical, measuring, and control systems.

Following the general guidelines laid down in applicable normative documents, the authors designed the required functionality of the test system including:
– enclosure, casing and sealing tests to ensure failure-free operation of mechanical and electric devices exposed to dust;
– electric enclosure dust tightness tests – determination of the degree of protection against dust penetration (IP code);
– operational reliability tests carried out on firearms exposed to dust;
– packaging, casing and personal protection equipment dust tightness tests; and
– automotive industry component dust tightness tests.
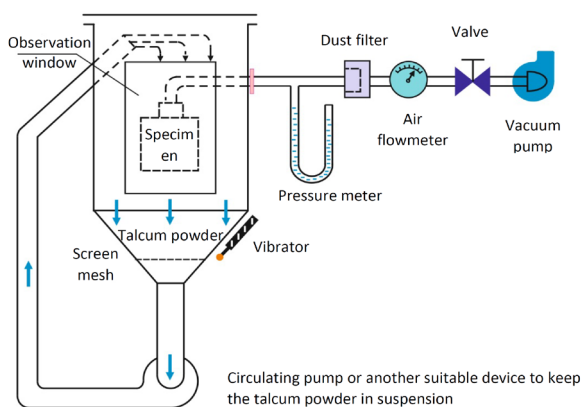
Fig.1. Structural diagram of the test system in accordance with the PN-EN 60529:2003 standard

The specimen is placed in a tight dust chamber with an observation window. The test consists in exposing the specimen to dust suspended in the air blown onto the enclosure. The amount of the dust to be used is 2 kg per cubic metre of the test chamber volume. The circulating air passes through a square-meshed sieve with the nominal wire diameter of 50 μm and the nominal width of the gap between wires of 75 μm. To avoid dust deposition on chamber components, vibrators are placed in key areas (diagonal wall, sieve enclosure). Where tests are carried out on enclosures inside of which, in the normal working cycle, the air pressure is below that of the surrounding atmospheric pressure, a vacuum pump is used to extract the air from the enclosure at a predefined extraction rate and pressure.

In accordance with the adopted functionality, the authors defined detailed technical parameters, both general (Table 1) and with reference to structural materials ensuring failure-free operation.

Table. 1. Basic technical parameters of the test system

Parameter	Value
Test area dimensions	1000 x 1000 x 1000 mm
Velocity of dust-filled air movement	<1 m/s
Dust type	talcum powder
Dust granularity	<75 μm
Partial vacuum	<2 kPa
Extraction rate	<60 enclosure volume per hour

Structural model

The construction of test devices that enable the simulation of conditions in which objects are exposed to dust causes a lot of problems that mainly concern the proper dosage of dust and the control over the amount of the agent used [3]. Given the scope of the recreated parameters, test devices are modular in structure, which enables flexible adaptation of their operating properties by means of an exchange of individual modules or their structural modification.

The test device described in this article is composed of the following functional modules:
– the process chamber;
– the air circulation system;
– the dust dosage system;
– the enclosure; and
– the control system.

In the process chamber, the specimen is exposed to dust in controlled dustiness, temperature and humidity conditions. The air circulation system ensures proper air circulation inside the dust chamber and even distribution of dust. The dust dosage system helps to keep the dust dry and to maintain it in suspension. At the same time, the measuring system controls the amount of dust in the tank and enables the use of a feedback loop. The device has a frame onto which individual modules and enclosure elements preventing dust outflow to the external atmosphere are mounted.

3D model

At the concept stage, the authors defined user software and hardware requirements and on that basis developed in the CAD environment the structural geometric 3D model enabling computer visualisation and simulation. The 3D model has a modular structure complying with the specification of the structural model.

The 1 m³ process chamber was designed as a thin-walled sheet metal structure and it was equipped with a steel grating on which the specimen is placed (Fig. 2). In the chamber walls, process connections and LED illuminators are mounted.
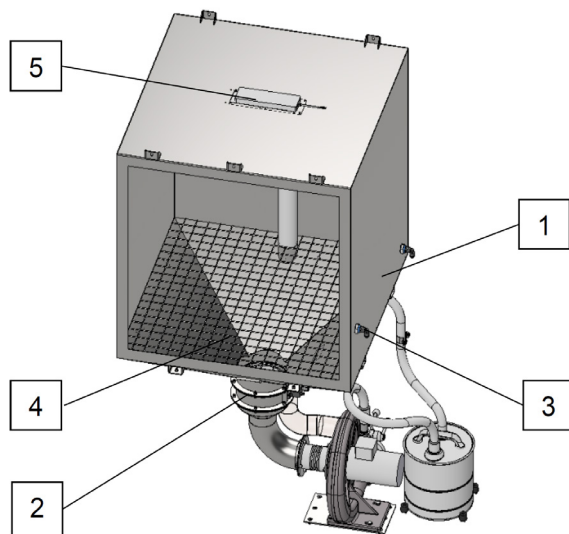
Fig. 2. Process chamber 3D model: 1 – casing; 2 – hopper; 3 – connections; 4 – grating; 5 – illuminator

The hopper connects the chamber with the air circulation system (Fig. 3) composed of the process and dust extraction circuits (Fig. 4). The process circuit is made of modules connected in series that include: filtration, blower with connections, stream separating valves, and dust ducts. The dust extraction circuit is intended to extract the used (polluted) dust and it is composed of the dust separator and flexible cords. To switch from one circuit to another, the separating valves need to be turned manually. The dust is transported using a side channel blower, the speed of which is controlled with an inverter.

The dust (talcum powder) with defined granularity is placed in the dose tank (Fig. 4). The 3 dm³ tank with supports at the bottom is placed on three weight sensors that enable dust use monitoring. To eliminate clumping, four foil heaters and a vibrator are used – the first heat the dust and reduce humidity, while the latter keeps the dust in suspension and prevents its deposition.

Dust is supplied through an ejector. As regards the weighing system, the operations of equalisation, calibration, taring and reading conversion into dust mass were applied. After the tank is filled with dust, the weighing
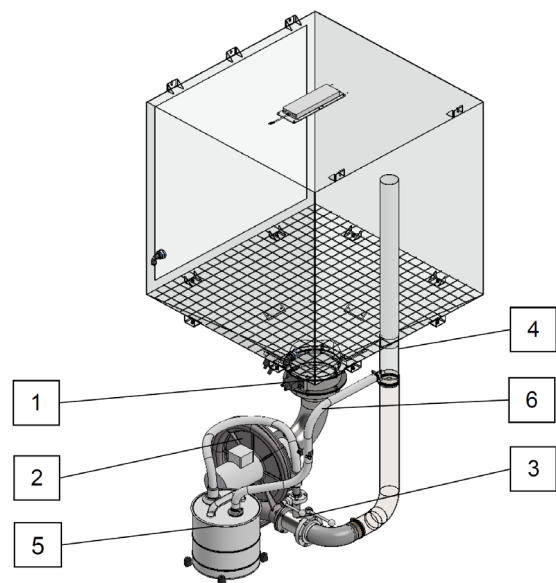
Fig. 3. 3D model of the air circulation system: 1 – filter; 2 – blower with connections; 3 – valves; 4 – dust duct; 5 – dust separator; 6 – flexible cords
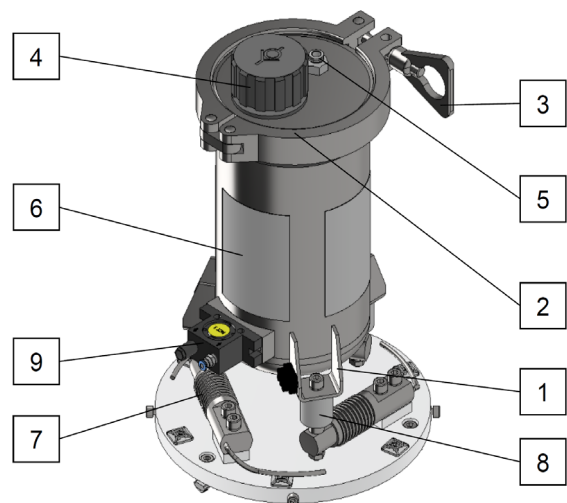
Fig. 4. 3D model of the dust dosing module (view without casing): 1 – tank; 2 – cover; 3 – clasp; 4 – breather valve; 5 – suction connection; 6 – heater; 7 – weighing sensor; 8 – vibration isolator; 9 – vibrator

system needs to be tared to establish how much talcum powder or other agent has been placed in the tank. The ejector cyclically doses the required dust mass. The user enters the dosing and interval times in seconds – the process lasts until the specified mass is obtained.

All modules were mounted onto a frame made of aluminium profiles. For ergonomic reasons, the dust chamber was mounted on a level enabling its manual operation. Below the chamber, the dust dosage and air circulation modules were fixed (Fig. 5).
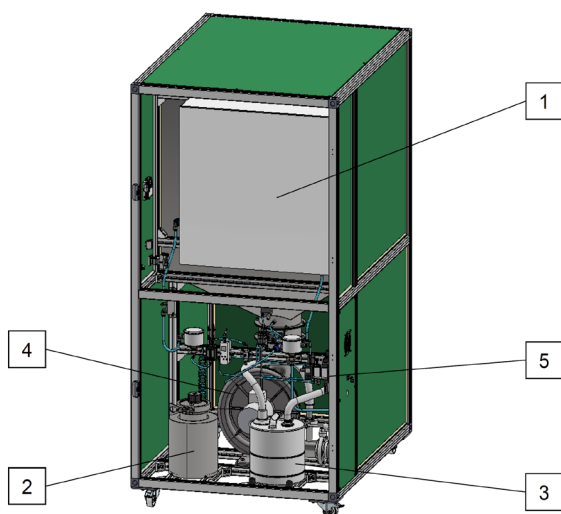
Fig. 5. 3D model of the dust chamber: 1 – control panel cabinet; 2 – dust dosage module; 3 – separator; 4 – blower; 5 – control element

Fig. 6. Chamber prototype: a) front view; b) air circulation system dust dosage system; c) control panel

Measuring and control system

Based on the adopted structure, the authors developed the algorithmic model of the control system, taking into consideration information processing circuits as well as the hardware and software layers. The measuring and control elements were selected in accordance with the 24VDC standard for binary signals, the 4-20mA/0-10V standard for analogue signals and Modbus RTU communication protocol. The HG2G touch user interface communicates with PLC resources via Ethernet. The PLC, HMI, and the external computer are connected to a switch.

In the measuring and control system the IT system was divided into software modules for analogue blocks, alarms, and modules controlling individual functional modules of the chamber.

The software is of hybrid nature and combines several programming paradigms. The PLC and HMI software resources enable so-called systematic programming. The HMI software has the characteristics of so-called object--oriented programming. Additionally, in the user interface, the authors used scripts to facilitate the preparation and use of the PLC recording resources. A modular, asynchronous architecture of the chamber software in the PLC was assumed. Flags (so-called relays type M) activate and synchronise the individual modules in line with the idea of distributed software.

Prototype verification

The prototype dust chamber was built based on the adopted assumptions and the developed model. The prototype was equipped with a complete set of instrumentation to verify the correct operation of the individual units (Fig. 6).

The verification and validation tests were carried out in the actual operational environment [13]. During the tests trial technological processes were performed. The test results enabled the authors to evaluate the technical solutions used and to verify all technical documentation drafted.

From the verification it followed that the dust dosage process was not effective enough, which was mainly caused by the inappropriate length of the ejector's suction and delivery hose. This led to a significant drop in partial vacuum, as a result of which the suction force was too weak to extract the dust from the tank. Moreover, the insufficient effectiveness of the dust dosage process was also caused by the inadequate performance of

a)

b)

the breather valve located in the chamber's casing. As a result of the ejector's operation, relative pressure was created, which prevented dust ejection on the discharge side.

Prototype verification tests ended with a trial dust tightness test carried out on the complete enclosure with control systems (Fig. 7).

The prototype allowed the authors to carry out the planned tests in keeping with normative requirements. The enclosure proved tight and no dust was found inside it.

Conclusions

Test system to verify the degree of protection against dust penetration enables enclosure dust tightness tests to be carried out in accordance with normative requirements. The developed hardware and software architecture also allows tests to be carried out under expanded conditions defined individually to imitate the actual operational environment. Talcum powder or another agent (e.g. sand or ash) with granularity enabling the discharge fluidization and dust cloud creation can be used as dust.

As a result of the prototype verification the authors were able to identify structural issues and implement relevant corrective actions. From the enclosure tests it followed that the system is suitable for the determination of the degree of protection against dust penetration.

References

[1] Dudek J. 2014. „Pył węglowy – demonizacja problemu czy realne zagrożenie w energetyce przesyłowej?". Bezpieczeństwo Pracy: nauka i praktyka 8: 19–21.

[2] Kałuża G. 2013. Stopień ochrony ip zapewniany przez obudowy urządzeń przemysłowych. Zeszyty Problemowe – Maszyny Elektryczne 2(99): 317–323.

[3] Mizak W., Mazurkiewicz A., Smolik J., Zbrowski A. 2014. "Problems with abrasive dosing in erosive wear process modelling". Eksploatacja i Niezawodność – Maintenance and Reliability 16(4): 559–564.11

[4] NO-10-A500-6:2000 „Broń strzelecka. Metody badań. Badanie działania w warunkach pyłu". Ministerstwo Obrony Narodowej.

[5] PN-EN 60529:2003 Stopnie ochrony zapewnianej przez obudowy (Kod IP).

[6] Pracht M., Stępniak W., Wróblewski A. 2014. „Analiza i synteza metodyk badawczych broni strzeleckiej na przykładzie testów pyłoszczelności karabinków". Problemy Techniki Uzbrojenia 43(129): 67–74.

[7] Stępniak W., Badurowicz P. 2017. „Oczekiwane cechy konstrukcyjne nowego polskiego pistoletu wojskowego". Problemy Techniki Uzbrojenia 46(141): 95–115.

[8] Szczepankowski A., Szymczak J. 2011. „Wpływ zapylonego otoczenia na charakterystyki i parametry pracy lotniczych silników turbinowych". Journal of KONBiN 1(17): 257–268.

[9] Wnęk W., Jargieło M., Porowski R. 2016. „Wpływ pyłów pochodzenia drzewnego na działanie czujek pożarowych dymu". Bezpieczeństwo i Technika Pożarnicza 42(2): 43–55.

[10] Wnęk W. 2011. Rodzaje fałszywych alarmów i źródła ich powstawania, Warsztaty Zacisze: Czynniki wpływające na niezawodność instalacji sygnalizacji pożarowej. Tom XIX: 7–13.

[11] Zbrowski A., Mizak W. 2011. „Analiza systemów wykorzystywanych w badaniach uderzeniowego zużycia erozyjnego". Problemy Eksploatacji 3: 235–250.

[12] Zbrowski A., Samborski T., Kozioł S. 2014. „Analiza czynników środowiskowych oddziałujących na rogatki kolejowe". Logistyka 6: 11734–11739.

[13] Zbrowski A. 2016. Metodyka badań prototypów i jednostkowych urządzeń technicznych. Radom: Wydawnictwo Naukowe ITeE – PIB.

inż. Stanisław Kozioł
stanislaw.koziol@itee.lukasiewicz.gov.pl;

dr inż. Tomasz Samborski
tomasz.samborski@itee.lukasiewicz.gov.pl

mgr inż. Mariusz Siczek
mariusz.siczek@itee.lukasiewicz.gov.pl

dr hab. inż. Andrzej Zbrowski
andrzej.zbrowski@itee.lukasiewicz.gov.pl

Sieć Badawcza Łukasiewicz – Instytut Technologii Eksploatacji

YOUNG'S MODULUS OF A CARBON-REINFORCED COMPOSITE AT AN ELEVATED TEMPERATURE

Moduł Younga kompozytu wzmacnianego włóknami węglowymi w podwyższonej temperaturze

Robert SZCZEPANIAK   ORCID: 0000-0003-3838-548X

Paweł PRZYBYŁEK   ORCID: 0000-0002-7544-3813

Andrzej KOMOREK   ORCID: 0000-0002-2293-714X

Przemysław SAPIŃSKI   ORCID: 0000-0002-3974-7676

Artur ROWICKI

Sławomir TKACZUK   ORCID: 0000-0001-9546-4278

Andrzej RYPULAK   ORCID: 0000-0003-3671-661X

Sebastian STABRYN   ORCID: 0000-0001-5994-9075

Abstract: Aviation structures are operated under varying environmental conditions, affecting the properties of polymer composites, which are often used to manufacture components for airplanes and helicopters. One of such factors is an operating temperature that changes during a flight in a very wide range. This paper presents the influence of an operating temperature upon composite properties determined during a tensile test. In addition, composites which are intended for the research were post cured during their preparation at different temperatures (in accordance with the recommendations of the resin manufacturer which constitutes a matrix base). The composites consisted of 7 layers of carbon fabric, and matrix of L285 epoxy resin, with a hardener. As a result of the testing it was noted that a change in the operating temperature exerts a significant effect on composite strength properties regardless of the post curing temperature. The materials post cured at higher temperatures were characterized by a greater value of the modulus of elasticity and tensile strength.

Keywords: tensile test, CFRP, *Young's* modulus, static strength

Streszczenie: Konstrukcje lotnicze są eksploatowane w zmiennych warunkach środowiskowych wpływających na właściwości kompozytów polimerowych, z jakich często wykonywane są elementy samolotów i śmigłowców. Jednym z takich czynników jest temperatura użytkowania, zmieniająca się podczas lotu w bardzo szerokim zakresie. W artykule zaprezentowano wpływ temperatury eksploatacji na właściwości kompozytu wyznaczane podczas próby rozciągania. Dodatkowo kompozyty przeznaczone do badań wygrzewano w trakcie przygotowania w różnych temperaturach (zgodnie z zaleceniami producenta żywicy będącej osnową). Kompozyty składały się z 7 warstw tkaniny węglowej przesyconych żywicą epoksydową L285 z utwardzaczem. W wyniku badań zauważono, że zmiana temperatury eksploatacji wywiera istotny wpływ na właściwości wytrzymałościowe kompozytu bez względu na temperaturę wygrzewania. Materiały wygrzewane w wyższych temperaturach cechowała większa wartość współczynnika sprężystości wzdłużnej i wytrzymałości na rozciąganie.

Słowa kluczowe: próba rozciągania, kompozyt ze wzmocnieniem węglowym, moduł *Younga*, wytrzymałość statyczna

Introduction

The search for novel material solutions, enabling the rise of utility performance parameters of products, taking into account the economic and ecological aspects, is one of the main objectives of materials engineering. Composites as construction materials offer the designers a combination of properties not available in traditional materials [1, 13]. Low production costs and high strength made composites extremely common. For this reason, composites are particularly eagerly used by designers of various means of transport [5, 8], where by reducing weight, greater ranges, lower fuel consumption and greater transport possibilities are obtained.

The composites are used in aviation, both in the production of light aircraft e.g. gliders but also in the structures of civil aircraft and military aircraft [3, 11]. During flights many planes take to high altitudes, and as altitude increases, the outside temperature drops. In turn, jet airplanes (especially military ones) and spacecraft achieve high speeds during flight, and their fuselages and other external elements may heat up due to friction [9]. So a lot of aircraft's elements operate at different temperatures that may cause changes in their mechanical properties. Nowadays one of the most frequently used reinforcements in polymer composites used in aviation are carbon fibers [2]. Since the potential change in the mechanical properties of the material along with the temperature of use is a significant problem in aircraft structures, the authors decided to carry out strength tests as a function of different operating temperatures of carbon fibers. Additionally, taking into account the recommendations of

the manufacturer of the composite matrix material [6], the influence of the post-curing temperature of the material at the stage of its production on the modulus of elasticity was determined. When designing various structures, including aircraft, the mechanical properties of materials play a very important role. If these properties change during operation, the structure may be damaged or even destroyed. One of the most important material mechanical properties of construction materials is the modulus of elasticity, therefore this physical quantity was analyzed in the research presented in the article.

The test examination was a static tensile test [7]. Each sample from a batch was heated up at a different temperature. During the test, the samples were subjected to a constant temperature, simulating a heightened temperature of operation.

Research methodology

In order to conduct the test, the authors prepared composite panels, which were then used to cut out samples. The composite reinforcement was a carbon-fiber fabric GG 416 P/T, 416 g/m² in weight, with a double weave. The laminate consisted of seven layers.

The matrix base was made up of epoxy resin L285 with H285 hardener, in accordance with the manufacturer's recommendations, mixed in 100:40 weight ratio. In order to meet the design requirements during the construction of gliders and motor gliders, resin should be post cured at a temperature of 50–55 °C. If the resin is to be used to build engine aircraft, it should be post cured at a temperature of 80°C. The temperature range in which no significant changes in the properties of the resin are observed is included between -60°C to 50–60 °C without post curing, and between –60°C to 80–100°C for a post cured material.
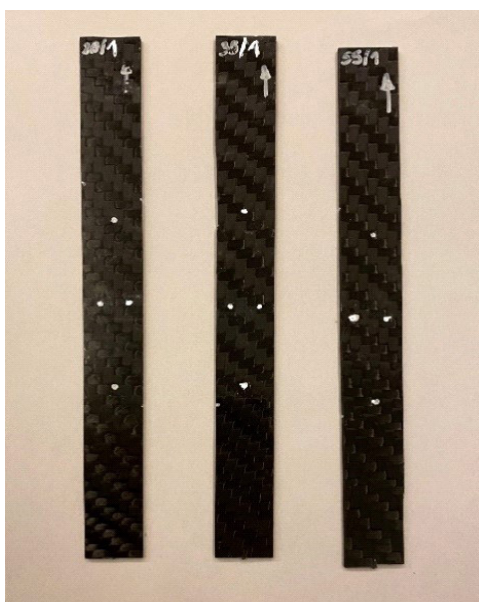
In order to remove any air bubbles from the composition, after mixing the components, the authors removed gas in an ultrasound bath for five minutes. Then the layers were put together and laid down in a hydraulic press. They were exposed to a load of 30 tonnes. The obtained material was used for the preparation of rectangular samples for the tests, sized 280 x 25 x 2.5 mm, in accordance with the EN ISO-527 standard [4]. The samples were cut out by means of the waterjet method.

The prepared sample (Fig. 1) were exposed to the process of post curing in a climatic chamber, manufactured by Weiss WKL 64. Each batch was post cured at a different temperature: 35, 55, 80 and 100°C for 24 hours, respectively.

The tests were conducted by means of the Instron 5982 Testing System with an optical tensometer, additionally equipped with SF-16 resistance furnace. The traverse movement was 2 mm/min during the tests.

In the first stage, the bearing capacity of the prepared samples was determined. For this purpose, a batch of samples, not subjected to post curing, was used. The average bearing load of the examined sample batch amounted to 44 kN. It was decided to continue using tensile load of 25 kN in proper research. In accordance with the adopted methodology, the sample was inserted in a resistance furnace and heated up to a set temperature. It was stabilized at this temperature for 5 min. The loading was increased up to 25 kN (Fig. 2).
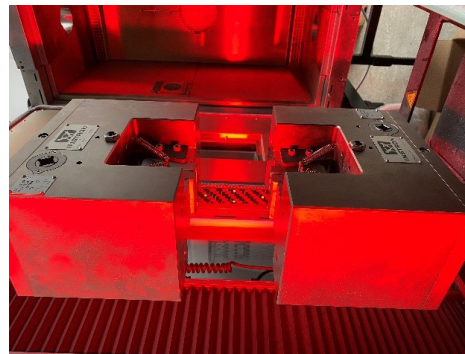
Fig. 2. Strength testing machine with a chamber furnace ready for research

Fig. 1. Test samples

Research results

The test results of the composite cured at room temperature prove that along with a temperature increase during an examination, there is an almost linear decrease in the value of *Young's* modulus (Fig. 3).
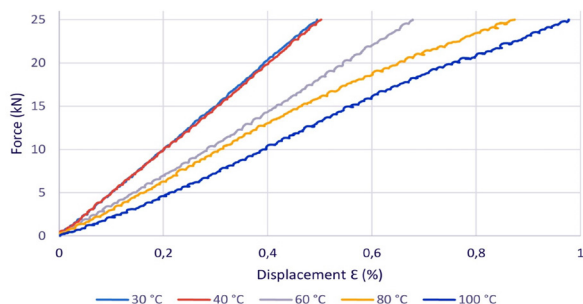
Fig. 3. Tensile test curves of samples cured at room temperature

Table 1. *Young's* modulus values which are dependent upon temperature for the composite cured at room temperature

Temperature (°C)	30	40	60	80	100
Modulus of elasticity (GPa)	75.45	74.65	62.01	53.62	47.80

The results of the composite cured at room temperature are shown in Table 1. Up to the temperature of 40°C, no change in *Young's* modulus was observed (Fig. 4). However, above this temperature a steady decline in the modulus value is noticeable, by 47.80 GPa for the temperature 100°C.
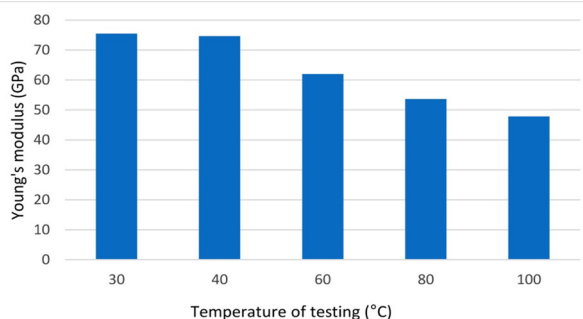
Fig. 4. *Young's* modulus of the composite hardened at ambient temperature

Increasing the temperature of testing composites post cured at 35°C, similar to a non-post cured composite, causes an almost linear decrease in *Young's* modulus (Fig. 5, 6). It seems that values close to the value of the modulus of elasticity during an examination at 30°C

and 40°C may be due to a slight increase in temperature. They do not entail changes in the structure of the composite matrix base. At higher research temperatures, there was a decline in *Young's* modulus to a value of 51.91 GPa for the temperature 100°C (Table 2), i.e. by 28%.

Table 2. *Young's* modulus values which are dependent on a temperature for the composite post cured at 35°C

Temperature (°C)	30	40	60	80	100
Young's modulus (GPa)	72.81	71.02	62.38	58.08	51.91
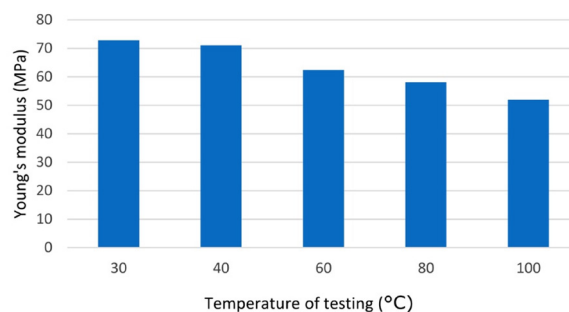
Fig. 5. *Young's* modulus of composite post cured at 35°C
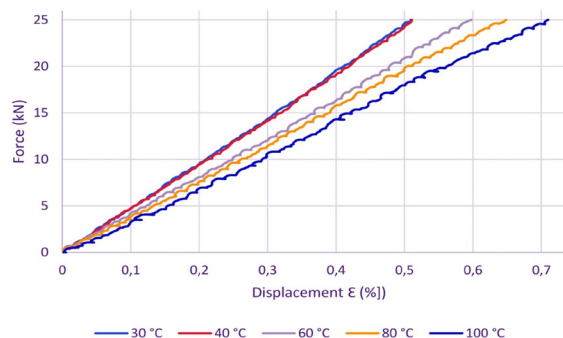
Fig. 6. Tensile test graph of samples post cured at 35°C

The examinations of the samples post cured at 55°C show a drop in *Young's* modulus along with increasing the examination temperature. *Young's* modulus changes in a linear manner, from 76 to 63.18 GPa (Fig. 7), yet its drop is lower than for samples post cured at a lower temperature.

Table 3. *Young's* modulus values which are dependent on temperature research for the composite post cured at 55°C

Temperature (°C)	30	40	60	80	100
Young's modulus (GPa)	76.49	76.8	73.67	69.39	63.18

Fig. 7. *Young's* modulus of samples post cured at 55°C
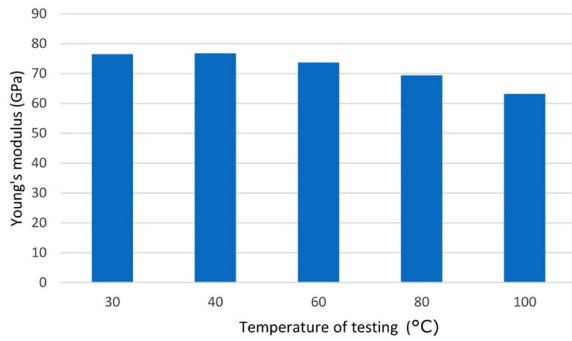
Fig.9. *Young's* modulus of samples post cured at 100°C

The examination carried out for the samples post cured at 80°C demonstrates that the elasticity modulus initially rose at 40°C, and then, at a further temperature rise, its value was lowered. The highest value of *Young's* modulus equalled 72.3 GPa (for the research temperature of 40°C), and the lowest was 59.61 GPa (for the research temperature of 100°C) (Fig. 8).

Table 4. Dependence between *Young's* modulus values and research temperature for the composite post cured at 80°C

Temperature (°C)	30	40	60	80	100
Young's modulus (GPa)	68.55	72.3	68.41	66.66	59.61
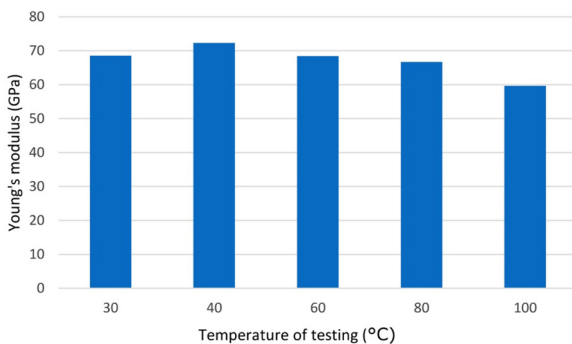
Fig. 8. *Young's* modulus of samples post cured at 80°C

No significant differences of *Young's* modulus were observed for samples post cured at 100°C during tests conducted at 30, 60, 80°C (Fig. 9). During a test at a temperature of 40°C, the value of *Young's* modulus exceeded 6%, whereas at 100°C it was over 8 % lower than *Young's* modulus, determined at 30°C. The changes can also be observed on a graph displaying a static tensile test of the sample (Fig. 10).

Table 5. Dependence between *Young's* modulus values and research temperature for the composite post cured at 100°C

Temperature (°C)	30	40	60	80	100
Young's modulus (GPa)	83.95	89.60	84.71	81.47	76.86
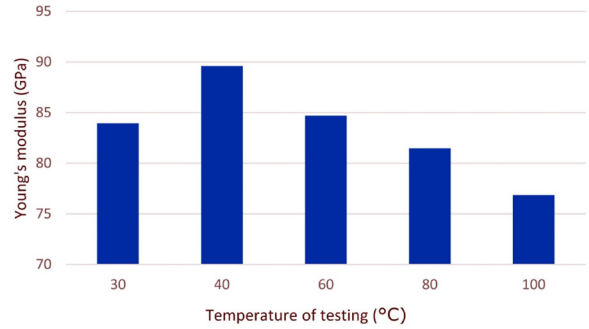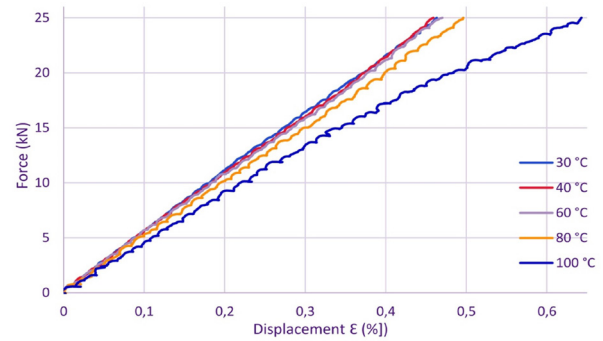
Fig. 10. Graph of a tensile test of samples post cured at 100°C was

Young's modulus value depended on temperatures, in which the composite was post cured (Fig. 11). Batch samples post cured at 100°C are characterized by the highest value of *Young's* modulus, regardless of the test temperature. Batch samples which were post cured at ambient temperature and at a temperature of 35°C are characterized by similar values (the differences do not exceed 5 GPa). The most stable value of *Young's* modulus is characterized by samples post cured at 55°C (changing the value is approximately 10 GPa for the whole range of the research temperatures). On the other hand, the biggest changes were observed for the material cured at room temperature.
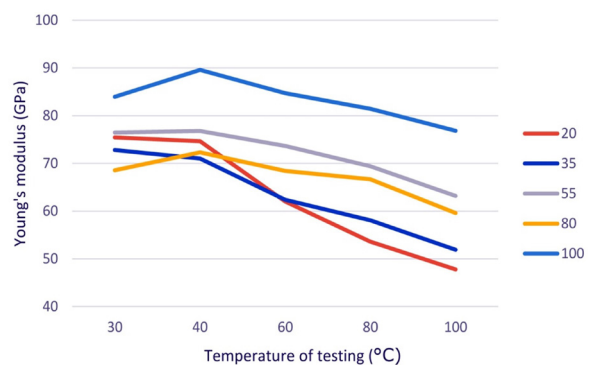
Fig. 11. *Young's* modulus in a function of temperature for all batches

After the tests were carried out in the thermal chamber, all the samples underwent full tensile tests. Examples of stress-strain curves after temperature testing are shown in Fig. 12. The highest bearing capacity (approximately 47 kN) was observed in samples post cured at 55°C and 80°C. It needs to be noted that these are the temperatures recommended by the resin manufacturer. The sample post cured at 80°C was also characterized by the highest value of relative deformation during the destruction - the lowest deformation during destruction demonstrated the sample post cured at 100°C, in which the highest value of *Young's* modulus is visible.
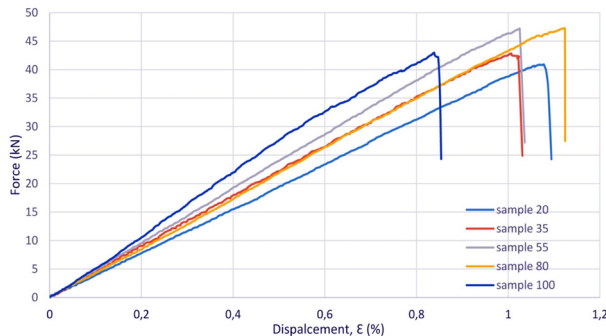
Fig. 12. Tensile test curves of selected samples after temperature tests

Conclusions

Based on the analysis of the results of the conducted research, the following conclusions were formulated:

1. The tests carried out have shown that the temperature change has a significant impact on the strength properties of the composite. Both the post-curing process and the thermal conditions of the exploited composite affect its strength.

2. Post-curing at higher temperatures increases the modulus of elasticity, which is important in aircraft structures [10, 12]. The highest value of this coefficient, regardless of the test temperature, has a composite hardened at a temperature of 100°C, which shows that when recommending the value of the post-curing temperature, the manufacturer was not guided solely by the value of Young's modulus.

3. The majority of the examined composites were characterized by the highest value of the modulus of elasticity during the tests at 40°C, the process of post curing the sample increases the tensile strength of the examined composites, after the entire testing cycle, the samples post cured at 55°C (recommended for gliders) and at 80°C (recommended for engine aircraft) had the highest bearing capacity.

References

[1] Alabtah F., Mahdi E., Eliyan F. 2021. The Use of Fiber Reinforced Polymeric Composites in Pipelines: A Review. Composite Structures. 276. 114595. 10.1016/j.compstruct.2021.114595.

[2] Banisaukas J., Shioleno M., Levan Ch., Rawal S., Silverman E., Watts R. 2005. Carbon Fiber Composites for Spacecraft Thermal Management Opportunities. AIP Conference Proceedings. 746. 10-21. 10.1063/1.1867113.

[3] Gay D. 2015. Composite materials: Design and applications. 3rd ed. CRC Press/Taylor & Francis Group.

[4] ISO 527-1:2019 Plastics — Determination of tensile properties.

[5] Koštial P., Koštialová-Jančíková Z., Ružiak I., Gajtanska, M. 2020. "Case Study of Chosen Sandwich-Structured Composite Materials for Means of Transport". Coatings 10: 750. https://doi.org/10.3390/coatings10080750.

[6] Laminating Resin MGS L285; Hexion Speciality Chemicals GmbH: Stuttgart, Germany. 2016. Available online: https://m.aircraftspruce.com/catalog/pdf/mgs285tech.pdf.

[7] Lomov, S.V., Ivanov, D., Truong, T.C., Verpoest, I., Baudry, F., Vanden Bosche, K., Xie, H. 2008. Experimental methodology of study of damage initiation and development in textile composites in uniaxial tensile test. Composites Science and Technology 68(12): 2340–2349. https://doi.org/10.1016/j.compscitech.2007.07.005.

[8] Mistry P., Johnson M., Galappaththi U. 2021. "Selection and ranking of rail vehicle components for optimal lightweighting using composite materials". Proceedings of the Institution of Mechanical Engineers, Part F: Journal of Rail and Rapid Transit. 235(3):390–402. doi:10.1177/0954409720925685.

[9] Reznik S. 2018. Thermal regimes of space composite structures. Part I, MATEC Web of Conferences 194, 01048, https://doi.org/10.1051/matecconf/201819401048.

[10] Scheuring, J.N., Grandt, A F. 1997. "Mechanical Properties of Aircraft Materials Subjected to Long Periods of Service Usage". J. Eng. Mater. Technol. 119(4): 380–386, https://doi.org/10.1115/1.2812273. [11] Swornowski P. 2010. „Kompozyty węglowe i szklane we współczesnym lotnictwie". Mechanik 1: 44–50.

[12] Szczeciński S. 2009. „Zagadnienia napędów lotniczych". Prace Instytutu Lotnictwa 4 (199).

[13] Tunali A. 2013. "Advanced Composite Applications in the Construction Industry". Polymers and Polymer Composites 21(3):195–198. doi:10.1177/096739111302100313.

Ph.D. Eng. Robert Szczepaniak – Faculty of Aviation, of the Air Force University in Dęblin
Dywizjonu 303 35, 08-521 Dęblin
e-mail: r.szczepaniak@law.mil.pl

Ph.D. Eng. Paweł Przybyłek – Faculty of Aviation, of the Air Force University in Dęblin
Dywizjonu 303 35, 08-521 Dęblin
e-mail: p.przybylek@law.mil.pl

Assoc. Prof., Eng. Andrzej Komorek – Department of Avionics and Control Systems, the Faculty of Aeronautics, of the Air Force University in Dęblin
Dywizjonu 303 35, 08-521 Dęblin
e-mail: komman@op.pl

MSc, Eng. Artur Rowicki, – Faculty of Aviation of the Air Force University in Dęblin
e-mail: artur.rowi@gmail.com

MSc, Eng. Przemysłąw Sapiński – Faculty of Aviation, of the Air Force University in Dęblin
Dywizjonu 303 35, 08-521 Dęblin
-mail: p.sapinski@law.mil.pl

Ph.D., Eng. Sławomir Tkaczuk – Institute of Aviation, in the Department of Mechatronics, Armament and Aviation at the Military University of Technology in Warsaw
Gen. S. Kaliskiego 2, 00-908 Warszawa
e-mail: slawomir.tkaczuk@wat.edu.pl

Ph.D. Eng. Andrzej Rypulak – Air Force University in Dęblin
Dywizjonu 303 35, 08-521 Dęblin

MSc. Eng. Sebastian Stabryn – Air Force University in Dęblin
Dywizjonu 303 35, 08-521 Dęblin

THE INFLUENCE OF THERMAL SHOCK ON THE LOAD CAPACITY OF CYLINDRICAL ADHESIVE JOINTS MADE OF EN AC-ALSI7-MG0.3 ALUMINUM ALLOY AND GLASS-EPOXY COMPOSITE EP405-GE

Wpływ szoków termicznych na nośność połączeń klejowych czopowych walcowych wykonanych ze stopu aluminium EN AC-AlSi7-Mg0.3 i kompozytu szkło-epoksyd EP405-GE

Władysław ZIELECKI   ORCID: 0000-0002-7864-5525
Przemysław BIELENDA
Ewelina OZGA   ORCID: 0000-0002-7359-6007

Abstract: The aim of the work was to investigate the effect of thermal shocks on the load capacity of cylindrical adhesive joints. The adhesive joints are made of ENAC-AlSi7Mg0.3 aluminum alloy (sleeve) and glass-epoxy compositeEP405-GE (pivot). The elements were joined together with the Araldite 2014 adhesive composition. The thicknesses of the adhesive layer were 0.025 mm, 0.075 mm or 0.125 mm. The adhesive joints were subjected to 0, 50, 100 or 150 cycles of temperature changes. The maximum temperature was 60˚C and the minimum temperature was -20˚C. The results of the strength tests show that in the accepted range of variability of input factors, subjecting the joints to thermal shocks had a positive effect on their load capacity. The highest values of load capacity were observed for joints with 0.125 mm or 0.075 mm thick adhesive layer, which were subjected to 150 cycles of temperature changes. According to the results of the regression and correlation analysis, within the adopted range of input factors variability, the number of cycles of temperature changes has a statistically significant influence on the load capacity. It has been shown that the load capacity of adhesive joints increases with an increase in the number of cycles of temperature changes. Student's t-test shows that statistically significant differences in the load capacity of adhesive joints subjected to a different number of thermal shocks cycles occur in the case of variants: G075L0 (adhesive layer thickness 0.075 mm, number of cycles 0) and G075L150 (adhesive layer thickness 0.075 mm, number of cycles 150) and variants: G125L0 adhesive layer thickness 0.125 mm, number of cycles 0) and G125L150 (adhesive layer thickness 0.125 mm, number of cycles 150).

Keywords: thermal shocks, cylindrical adhesive joints, aluminum alloy EN AC-AlSi7-Mg0.3, glass-epoxy composite EP405-GE

Streszczenie: Celem pracy była ocena wpływu szoków termicznych na nośność połączeń klejowych czopowych walcowych. Złącza klejowe wykonano ze stopu aluminium ENAC-AlSi7Mg0,3 (tuleja) oraz kompozytu szkło-epoksydowego EP405-GE (czop). Elementy połączono ze sobą za pomocą kompozycji klejowej Araldite 2014. Grubości utworzonych spoin klejowych wynosiły 0,025 mm, 0,075 mm i 0,125 mm. Połączenia klejowe poddano 0, 50, 100 lub 150 cyklom zmian temperatury. Temperatura maksymalna wynosiła 60˚C, a minimalna -20˚C. Wyniki badań wytrzymałościowych wskazują, że w przyjętym zakresie zmienności czynników wejściowych, poddawanie złączy szokom termicznym miało pozytywny wpływ na ich nośność. Najwyższe wartości nośności zaobserwowano w przypadku złączy ze spoiną o grubości 0,125 mm i 0,075 mm, które poddano 150 cyklom zmian temperatury. Zgodnie z wynikami analizy regresji i korelacji, w przyjętym zakresie zmienności czynników wejściowych, liczba cykli zmian temperatury ma istotny statystycznie wpływ na nośność połączeń. Wykazano, że nośność złączy klejowych rośnie wraz ze wzrostem liczby cykli zmian temperatury. Test t-Studenta wskazuje, że istotne statystycznie różnice w nośności połączeń poddawanych różnej liczbie cykli zmian temperatury występują w przypadku wariantów: G075L0 (grubość spoiny 0,075 mm, liczba cykli 0) i G075L150 (grubość spoiny 0,075 mm, liczba cykli 150) oraz wariantów: G125L0 (grubość spoiny 0,125 mm, liczba cykli 0) i G125L150 (grubość spoiny 0,125 mm, liczba cykli 150).

Słowa kluczowe: szoki termiczne, połączenie klejowe czopowe walcowe, stop aluminium EN AC-AlSi7-Mg0,3, kompozyt szkło-epoksydowy EP405-GE

Introduction

Adhesive technology is used in many different industries. The popularity of adhesive joints results from their numerous advantages, including the possibility of joining elements made of various materials, good damping and sealing properties, no need to make holes and possibility of reducing the weight of the structure [6, 14, 17]. Nevertheless, adhesive joints also have some disadvantages.

One of such disadvantages is the limited temperature resistance of adhesives [7].

The adhesives are of polymer nature. Therefore, the thermal properties of polymers influence the behavior of the adhesive joint at reduced, elevated or changing temperatures [4, 7]. Polymer materials (including adhesives) exposed to elevated temperatures are subject to the so-called thermal degradation. During degradation, macromolecules break down into smaller fragments. Increasing

the cross-linking of the material structure in the initial stage of degradation may lead to an improvement in its strength properties. However, further degradation progress, resulting in a reduction of the molecular weight or excessive cross-linking of the structure, may contribute to the reduction of the material strength [18].

The phenomenon of increasing the strength of adhesive joints under the influence of elevated temperature was investigated in [20]. The analyzes were carried out on the joints formed with the use of the adhesive composition with the optimal curing agent content, the composition with the excess curing agent and the composition with the curing agent deficiency. The joints were subjected to additional heat treatment at the stage of forming the adhesive joints. It was shown that heat treatment contributed to an increase in the static strength of connections at ambient temperature, regardless of the curing agent content in the adhesive composition. It has also been proven that heat treatment of joints with an excess of curing agent resulted in a decrease in the static strength of joints operated at elevated temperatures. Therefore, the authors of the research concluded that heat treatment (reheating) cannot be treated as a universal method of increasing the strength of adhesive joints.

Not only high, but also low temperatures can significantly affect the properties of adhesives. It was proved in [19] that negative temperatures increase the brittleness of epoxy compounds. For this reason, adhesives that are used at low temperatures are generally more plastic than those intended for use at elevated temperatures [5]. It was shown in [12] that low temperatures increase the stiffness of adhesive joints, while high temperatures reduce it.

In practice, adhesive joints are most often exposed to cyclical temperature changes. The problem of thermal fatigue caused by thermal shocks has been the subject of various studies [8–11, 13].

The work [11] analyzes the effect of thermal loads on the shear strength of 316L steel single lap adhesive joints connected with Hysol 9484 and Hysol 3421 adhesives. The adhesive joints were subjected to 200 cycles of temperature changes. The minimum temperature was -40°C and the maximum 60°C. The conditioning time of the samples at each temperature was 15 minutes. According to the test results, subjecting the samples to thermal shocks reduced the mean value of the shear stress. The highest, 30% decrease in shear stress value was observed for joints connected with Hysol 9484 with mechanically processed adhesive surfaces.

Similar studies are presented in [9]. The adhesive joints of 316L steel, connected with Epidian 5 and Epidian 6 epoxy adhesives hardened with Z1 and PAC curing agents, were subjected to 200 cycles of temperature changes in the range from -40°C to 60°C. As a result of the research, it was found that the adhesive compositions with the PAC curing agent had the highest resistance to thermal shocks. In turn, the greatest decrease in the value of shear stresses in the aftermath of temperature

changes was observed in the case of joints connected with the Epidian 5 + Z1 composition (about 50% decrease in shear stresses).

The subject of the work [8] was the analysis of the influence of cyclic temperature changes on the *Young's* modulus of adhesivecompositions based on Hysol 9466 and Hysol 3421 epoxy resin. The samples were subjected to 200 cycles of temperature changes. The minimum temperature was -40°C and the maximum 60°C. The author of the research showed that as a result of subjecting the samples to thermal shocks, the *Young's* modulus values decreased by 8% for Hysol 9466 and 20% for Hysol 3421.

The authors of the work [13] investigated the effect of thermal shocks on the interlayer adhesion of fiber-metal-laminate composites with a polymer-fiber layer used to make a glass fiber prepreg with a thermosetting epoxy matrix. The samples, depending on the variant, were subjected to 500 or 1000 cycles of temperature changes. The minimum temperature was -40°C and the maximum 60°C. It was observed that under the influence of thermal shocks the stiffness of the composite matrix and the strength of the interlayer adhesive joint decreased. It was found that differences in thermal expansion of composite components were the main reason for the reduction of the joint strength.

To sum up, the problem of the influence of thermal shocks on the strength properties of adhesive joints seems to be a very important issue in the design and operation of adhesive structures. In the literature, there are some analyzes concerning the influence of thermal shocks on the strength of adhesive joints. However, the results of these analyzes are partial and inconclusive. Moreover, most of the research was carried out on lap joints in which the same materials were joined together. Therefore, it is justified to conduct further research that would allow for a better understanding of the problem, explaining the mechanism of the phenomena, and most importantly, predicting the strength properties of adhesive joints subjected to thermal shocks. Therefore, the aim of the research presented in the article is to assess the impact of thermal shocks on the load capacity of cylindrical adhesive joints made of ENAC-AlSi7Mg0.3 aluminum alloy and glass-epoxy compositeEP405-GE. The adhesive joints examined in the article reflect the actual joints in composite overhead insulators. A more detailed description of the overhead composite insulators can be found in the works [3, 21]. This article is a continuation of the research presented in [21], which included the analysis of the effect of natural seasoning on the load capacity of cylindricaladhesive joints.

Methodology

The analysis of the impact of thermal shocks on the load capacity of adhesive joints was carried out for cylindrical joints. The sleeves were made of ENAC-AlSi-7-Mg0.3 aluminum alloy (Table 1). The pivots were made

Table 1. Chemical composition of ENAC-AlSi7Mg0.3 aluminum alloy [1]

Fe	Si	Mn	Ti	Cu	Mg	Zn	Others	
max 0.19	6.5 - 7.5	max 0.1	max 0.25	max 0.05	0.25 - 0.45	max 0.07	each 0.03; total 0.1	Al - balance

of EP405-GE glass-epoxy composite (manufacturer - KU-VAG ISOLA Composites GmbH, Germany).

The two-component composition Araldite 2014 (manufacturer – Huntsman, Germany) was used to make the adhesive joints. Araldite 2014 is resistant to temperatures up to 120˚C (248˚F), exposure to different chemicals and water. It can be used for bonding ceramics, metals, GRP structures, electronic components and other elements exposed to an aggressive environment and elevated temperature. The curing of the Araldite 2014 composition takes place at room temperature [2].

The surfaces of pivots and sleeves were mechanically treated in order to develop the geometrical structure of the surface and, as a result, to increase the strength of adhesive joints between the adhesive and the adherends.

The sleeve surfaces were turned on the LZ-360 universal lathe (manufacturer – Fabryka Maszyn Tarnów, Poland). The pivots surfaces were ground using a RUP-280 roller grinder (manufacturer – Fabryka Maszyn Tarnów, Poland) with an MVBE 45 grinding wheel with dimensions of 400x50x107 mm (manufacturer – Norton Saint-Gobain HPM Polska Sp. z o. o., Poland).

Then, the surface roughness of the adherends (sleeves and pivots) was measured. Measurements were carried out using an optical profilometerTalysurf CCI Lite (manufacturer –Taylor Hobson, England). The designations and the meaning of the surface roughness parameters were adopted in accordance with the PN-EN ISO 4287:1999standard [16].The results of the roughness measurements are presented in Table 2.

Table 2. Results of surface roughness measurements

SLEEVE (turned)								
2Dparameters								
Rp	Rv	Rz	Rc	Rt	Ra	Rq	Rsk	Rku
11.8 μm	7.51 μm	19.4 μm	17.7 μm	20.9 μm	4.64 μm	5.46 μm	0.579	2.00

3Dparameters						
Sq	Ssk	Sku	Sp	Sv	Sz	Sa
16.1 μm	0.853	3.10	63.1 μm	26.3 μm	89.5 μm	13.0 μm

PIVOT (ground)								
2Dparameters								
Rp	Rv	Rz	Rc	Rt	Ra	Rq	Rsk	Rku
9.88 µm	8.75 µm	18.6 µm	4.16 µm	18.6 µm	0.599 µm	1.14 µm	0.635	29.4

Length = 1.65 mm Pt = 31.1 µm Scale = 50.0 µm

3Dparameters						
Sq	Ssk	Sku	Sp	Sv	Sz	Sa
12.6 µm	-0.597	2.21	36.2 µm	40.8 µm	77.0 µm	10.8 µm
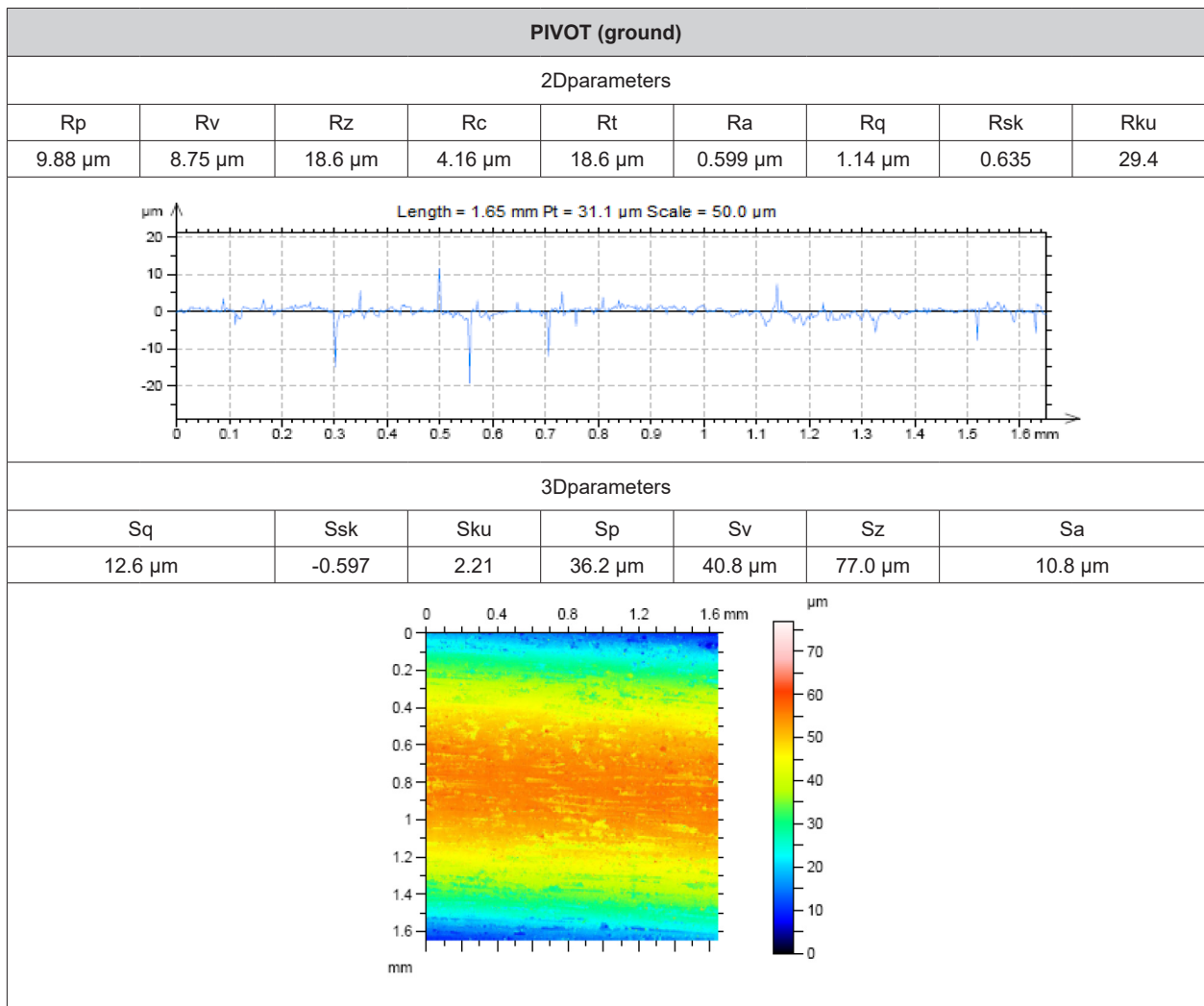
The next step was to degrease the surfaces of the adherends in order to remove grease contamination, dust and other machined residues that could weaken the connection. The pivots and sleeves were placed in an EMMI-40HC ultrasonic cleaner (manufacturer – EMAG, Poland) filled with acetone. After 5 minutes, the elements were removed from the washer and allowed to dry completely (the drying time was 5 to 10 minutes). The elements prepared in this way were bounded using the Araldite 2014 composition. A schematic drawing of the created cylindrical adhesive joints is shown in Figure 1.

The pivots diameter (d_1) was 16-0.01 mm. The inner diameter of the sleeves (d_2) was made in three dimensions: 16.05 mm, 16.15 mm, 16.25 mm so that it was possible to form joints with 0.025 mm, 0.075 mm or 0.125 mm adhesive layer thickness. The Araldite 2014 adhesive composition was applied to the inner surface of the sleeve and the central part of the pivot surface with a spatula. The sleeve was placed in the middle of the pivot. The sample prepared in this way was placed in a special device (jigging fixture). The device allowed to maintain the desired (coaxial) position of the joined elements and as a result the same thickness of the adhesive layer throughout the cross-section. The cross-linking process in the device was carried out for 48 hours at the temperature of 21 ± 1˚C. The scheme of the device used is presented in Figure 2.

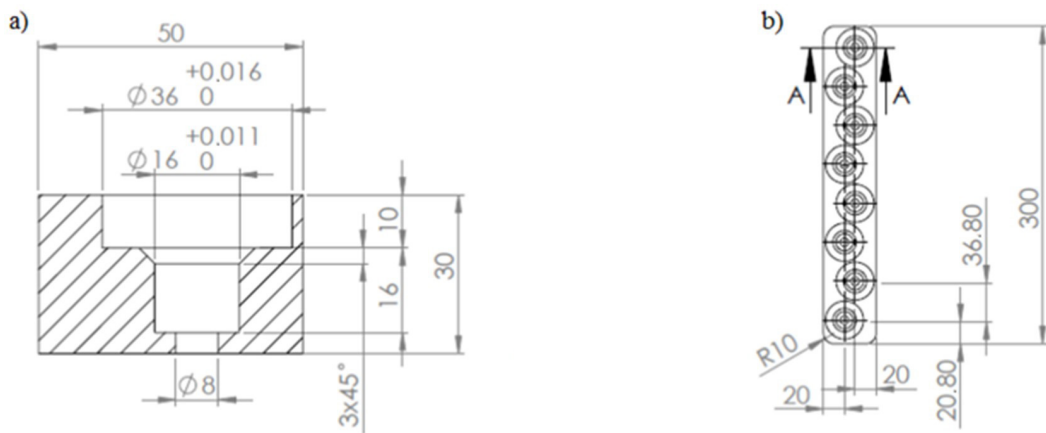Fig. 1. Dimensions and shape of the cylindrical adhesive joints

Fig. 2. Scheme of the device

The created adhesive joints were subjected to thermal shocks. For this purpose, the samples were alternately placed in a freezer (manufacturer – Electroline Equipment Inc, Canada) at a temperature of -20˚C and in a vacuum dryer (model DZ-2BC II, manufacturer – Huanghua Faithful Instrument Co., LTD, China) at a temperature of 60˚C. The samples were conditioned at each temperature for 30 min. Figure 3 shows the conditions of the conducted thermal shocks.
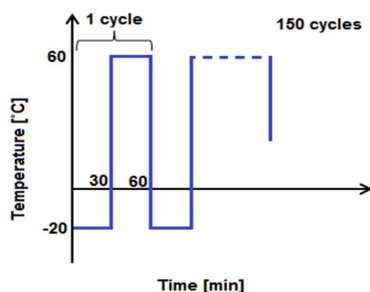
Fig. 3. Thermal shock conditions

Table 3. Variants of the created cylindrical adhesive joints

Serial No	Adhesive layer thickness [mm]	Number of cycles of temperature changes	Variant
1.	0.025	0	G025L0
2.		50	G025L50
3.		100	G025L100
4.		150	G025L150
5.	0.075	0	G075L0
6.		50	G075L50
7.		100	G075L100
8.		150	G075L150
9.	1.125	0	G125L0
10.		50	G125L50
11.		100	G125L100
12.		150	G125L150

After the samples were subjected to thermal shocks, 12 variants of adhesive joints were obtained. The variants differed in the number of cycles of temperature changes and the thickness of the adhesive layer. All variants are presented in Table 3.

The last step of the research was testing the strength of the cylindrical adhesive joints. The samples were subjected to an axial shear test on a Zwick/RoellZ100 testing machine (manufacturer: ZwickRoell GmbH & Co. KG, Germany). Figure 4 shows a sample placed in the handle of the machine.

Strength tests were carried out in accordance with the PN-EN ISO 10123: 2019-07 standard (Adhesives – Determination of shear strength of anaerobic adhesives using pin-and-collar specimens) [15]. During the tests, a test speed of 5 mm/min, initial force of 50 N and a maximum deformation of 15 mm were assumed

Fig. 4. The sample placed in the handle of the machine

Results and discussion

Table 4 and Figure 5 show the results of strength tests carried out for 12 variants of adhesive joints.

Table 4. Strength test results

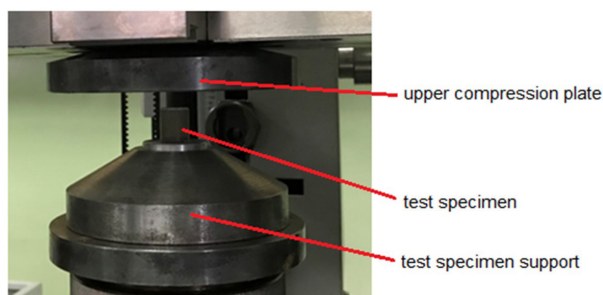| Variant	P₁[N]	P₂[N]	P₃[N]	P₄[N]	P₅[N]	P₆[N]	P₇[N]	P₈[N]	P₉[N]	P₁₀[N]	Loadcapacity – average P_śr[N]	Range R=Pmax-Pmin R[N]	Standard deviation σ[N]
G025L0	25112.71	28023.37	22261.08	20604.80	21862.16	20862.19	23167.45	26328.75	27845.20	22107.59	23817.53	7418.57	2799.67
G025L50	27333.71	21565.68	22055.58	25590.38	25708.87	26043.79	26261.69	27695.24	18858.11	29161.20	25027.43	10303.09	3192.66
G025L100	20752.99	28458.72	23907.96	24486.44	25619.28	27828.39	27247.12	26070.27	23514.06	26041.39	25392.66	7705.73	2304.23
G025L150	23589.24	21148.52	26880.74	26886.57	23588.71	23527.38	23314.81	22106.06	21882.15	26352.29	23927.65	5738.05	2090.88
G075L0	26208.53	24758.36	26444.87	13230.16	25911.43	19236.50	24745.84	25439.84	21089.39	24998.15	23206.31	13214.72	4210.60
G075L50	23903.23	29265.31	24718.64	29869.88	27519.99	18522.98	22706.30	24040.49	24446.96	21657.13	24665.09	11346.90	3464.64
G075L100	19799.32	19745.32	28628.21	24614.85	26061.77	29102.76	23783.63	26340.85	30129.65	26223.56	25442.99	10384.33	3575.48
G075L150	26191.64	25277.76	31584.72	31247.82	25219.04	26907.70	27265.66	22708.88	21483.75	24512.64	26239.96	10100.98	3252.13
G125L0	23956.96	24619.43	26665.20	19890.89	26199.82	20003.17	24916.84	22182.02	26355.67	25792.23	24058.22	6774.31	2539.92
G125L50	27476.50	27998.86	27112.49	25474.86	26347.16	25012.62	21656.53	23330.69	25026.18	25993.08	25542.90	6342.33	1933.17
G125L100	27659.24	24712.40	24113.39	23554.22	27813.81	29879.01	26365.35	23702.57	21413.58	23194.78	25240.83	8465.43	2600.04
G125L150	29733.20	27063.86	23856.34	26531.96	28482.58	24581.49	26540.47	25965.29	25084.13	27225.79	26506.51	5876.87	1769.85

Fig. 5. Strength test results

Table 5. The results of the analysis of significant differences between the load capacity of adhesive joints with different adhesive layer thickness

Number of cycles	Compared variants		p [%]
0	G025L0	G075L0	35.370
	G025L0	G125L0	42.135
	G075L0	G125L0	29.598
50	G025L50	G075L50	40.531
	G025L50	G125L50	33.430
	G075L50	G125L50	24.776
100	G025L100	G075L100	48.532
	G025L100	G125L100	44.582
	G075L100	G125L100	44.339
150	G025L150	G075L150	**3.880**
	G025L150	G125L150	**0.413**
	G075L150	G125L150	41.161

Table 6. The results of the analysis of significant differences between the load capacity of joints with 0.025 mm thick adhesive layer, which were subjected to 0, 50, 100 and 150 cycles of temperature changes

p [%]	G025L0	G025L50	G025L100	G025L150
G025L0	X	18.984	9.351	46.090
G025L50		X	38.647	18.804
G025L100			X	7.699
G025L150				X

Table 7. The results of the analysis of significant differences between the load capacity of joints with 0.075 mm thick adhesive layer, which were subjected to 0, 50, 100 and 150 cycles of temperature changes

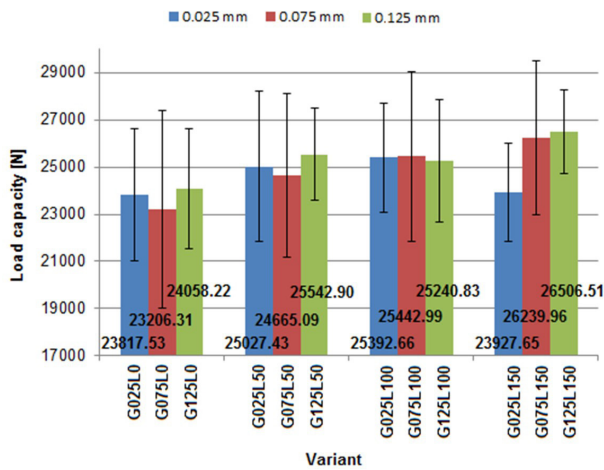| p [%]	G075L0	G075L50	G075L100	G075L150
G075L0	X	20.453	10.853	**4.460**
G075L50		X	31.361	15.427
G075L100			X	30.424
G075L150				X

Based on Table 4 and Figure 5, it can be concluded that the adhesive joints that have not been subjected to thermal shocks have the lowest load capacity. Adhesive joints with the same adhesive layer thickness, which were subjected to cyclical temperature changes, have a higher load capacity. Therefore, within the accepted range of variability of input factors, subjecting the adhesive joints to thermal shocks had a positive effect on their load capacity. The highest values of load capacity were observed for joints with 0.125 mm and 0.075 mm thick adhesive layer, which were subjected to 150 cycles of temperature changes. In the case of joints with 0.075 mm thick adhesive layer, it was noticed that the load capacity increases with an increase in the number of cycles. The increase in the load capacity of joints subjected to thermal shocks can be explained by the fact that high temperature could increase the cross-linking of the adhesive structure and stiffness of joints.

The results of the research on the influence of thermal shocks on the load capacity of cylindrical adhesive joints were statistically analyzed using the Student's t-test. Statistical significance α = 0.05 was assumed for the analyzes. Student's t-test was used to analyze significant differences between the load capacity of adhesive joints subjected to the same number of cycles of temperature changes, differing in the thickness of the adhesive layer. The results of the Student's t-test are presented in Table 5.

Based on Table 5, it can be seen that the probability values p are in most cases greater than 5%. Therefore, within the accepted range of variability of input factors, the compared variants of adhesive joints do not show statistically significant differences in terms of load capacity. Statistically significant differences in load capacity are revealed only between the pair G025L150 (adhesive layer thickness 0.025 mm, number of cycles 150) and G075L150 (adhesive layer thickness0.075 mm, number of cycles 150) and the pair G025L150 (adhesive layer thickness0.025 mm, number of cycles 150) and

G125L150 (adhesive layer thickness 0.125 mm, number of cycles 150). This means that only in the case of these two pairs, the thickness of the adhesive joint has a significant influence on the load capacity of the adhesive joints.

Student's t-test was also used to analyze significant differences between the load capacity of adhesive joints with the same thickness of the adhesive layer, but with a different number of cycles of temperature changes. The analyzes were performed for joints with 0.025 mm (Table 6), 0.075 mm (Table 7) and 0.125 mm (Table 8) thick adhesive layer.

Table 8. The results of the analysis of significant differences between the load capacity of joints with 0.125 mm thick adhesive layer, which were subjected to 0, 50, 100 and 150 cycles of temperature changes

p [%]	G125L0	G125L50	G125L100	G125L150
G125L0	X	7.990	15.858	**1.179**
G125L50		X	38.589	13.014
G125L100			X	11.076
G125L150				X

On the basis of Table 6, it can be concluded that all p values are greater than 5%. Therefore, within the accepted range of variability of input factors, in the case of adhesive joints with 0.025 mm thick adhesive layer, the number of cycles of temperature changes does not have a significant effect on their load capacity. According to the results presented in Table 7, only when comparing the variants G075L0 and G075L150 the p value is less than 5%. This means that within the accepted range of variability of input factors, a statistically significant difference in load capacity occurs in the case of joints with 0.075 mm thick adhesive layer, which were not subjected to cyclic

Table 9. Results of the one-way analysis of varianceANOVA

Input variable	Output variable	p
Adhesive layer thickness (ALT)	Load capacity (P)	0.480
Number of thermal shock cycles (CN)	Loadcapacity (P)	0.057

temperature changes or were subjected to 150 cycles of thermal shocks. A similar situation is observed in Table 8. According to the presented results, within the accepted range of variability of the input factors, a statistically significant difference in load capacity occurs only between joints with 0.125 mm thick adhesive layer, which were not subjected to thermal shocks or were subjected to 150 cycles of temperature changes.

The results of the strength tests were also subjected to the one-way analysis of varianceANOVA. This analysis was used to determine the extent to which the dependent variable (adhesive layer thickness or the number of cycles) affects the independent variable (load capacity). The results of the analysis are presented in Table 9.

The p values listed in Table 9. are greater than 0.05. This means that, according to ANOVA, both the thickness of the adhesive layer and the number of thermal shock cycles do not have a significant effect on the load capacity of the adhesive joints.

Subsequently, regression and correlation analysis was performed. The input factor was the thickness of the adhesive layer (ALT) or the number of thermal shock cycles (CN). The output factor was the load capacity of the adhesive joints. As a result of the conducted analyzes, regression equations were obtained. The equations show the relations between the load capacity and the adhesive layer thickness and between the load capacity and the number of thermal shock cycles. The calculated values of the Pearson's linear correlation coefficient (R) indicate the degree of linear dependence between the analyzed variables. The values of the determination coefficient R^2 specify the percentage of changes in the output variable resulting from changes in the input variable. The results of the regression and correlation analysis are presented in Table 10.

Table 10. Results of regression and correlation analysis

Input variable	Output variable	Linearregressionequation	Pearson's correlation coefficient R	Coefficient of determination R^2	p_1	p_2	p_3
ALT	P	$y_P = 24325 + 7958 \times ALT$	0.111	0.012	0.000	0.226	0.226
CN	P	$y_P = 24041 + 11.7 \times CN$	0.225	0.051	0.000	0.013	0.013

p_1 - probability value for the constant, p_2 - probability value for the coefficient for the adhesive layer thickness / number of cycles, p_3 - probability value for the regression equation

According to the results of the analysis presented in Table 10, the regression equation describing the relationship between the load capacity and the number of thermal shock cycles can be considered statistically significant ($p_3 < 0.05$). Moreover, both the constant value and the value of the coefficient at the number of cycles have a significant influence on the result of the regression equation. The value of the Pearson linear coefficient indicates

that the load capacity of adhesive joints increases with an increase in the number of thermal shock cycles. The regression equation describing the relationship between the load capacity of the joints and the adhesive layer thickness is not statistically significant ($p_3 > 0.05$). Therefore, the thickness of the adhesive layer does not significantly affect the load capacity of the adhesive joints.

Conclusions

1. In the adopted variability of input factors, subjecting the samples to thermal shocks contributed to the increase of the load capacity of the adhesive joints. The highest increase in load capacity, amounting to 13%, was observed in the case of joints with 0.075 mm thick adhesive layer, which were subjected to 150 cycles of temperature changes. The increase in the load capacity of joints subjected to thermal shocks can be explained by the fact that high temperature could increase the cross-linking of the adhesive structure and stiffness of joints.

2. The analysis of significant differences between the load capacity of adhesive joints with different adhesive layer thicknesses showed that within the adopted range of variability of the input factors, only joints with adhesive layer thickness of 0.025 mm and 0.075 mm, as well as, 0.025 and 0.125 mm, which were subjected to 150 cycles of temperature changes, differ significantly in terms of load capacity. Therefore, only in these two cases the thickness of the adhesive joint had a significant influence on the load capacity of the joints.

3. The analysis of significant differences between the load capacity of joints subjected to a different number of cycles of thermal shock showed that within the adopted range of variability of the input factors, statistically significant differences in load capacity occur only in the case of joints with 0.075 mm or 0,125 mm thick adhesive layer, which were not subjected to thermal shocks or were subjected to 150 cycles of thermal shock. Therefore, only in these cases the number of cycles of temperature changes had a significant impact on the load capacity of the adhesive joints.

4. According to the results of the regression and correlation analysis, the relationship between the load capacity of the adhesive joints and the number of cycles is statistically significant. The value of Pearson's linear correlation coefficient indicates that the load capacity of a connection increases with an increase in the number of cycles of temperature changes.

References

[1] Aluminium alloy EN AC-AlSi7Mg0.3 technical data, [access September 2021], http://www.steelnumber.com/en/steel_alloy_composition_eu.php?name_id=1225

[2] Araldite 2014 technical data, [access September 2021], http://www.adhesivehelp.com/productdatasheets/huntsman-a2014.pdf

[3] Bielecki J., Wańkowicz J. 2014. "Nieznormalizowane wymagania i kryteria oceny kompozytowych wsporczych izolatorów stacyjnych do sieci 110 kV i 220 kV". Przegląd Elektrotechniczny 10: 106–109.

[4] Comyn J. 2018. Thermal Properties of Adhesives. In da Silva L. F. M., Öchsner A., Adams R. D. (ed.) Handbook of Adhesion Technology, 459-487. Springer International Publishing AG.

[5] da Silva L. F. M, Adams R. D. 2007. "Joint strength predictions for adhesive joints to be used over a wide temperature range". International Journal of Adhesion & Adhesives 27 : 362–379.

[6] da Silva L. F. M., Öchsner A., Adams R. D. 2018. "Introduction to Adhesive Bonding Technology". In da Silva L. F. M., Öchsner A., Adams R. D. (ed.) Handbook of Adhesion Technology, 1-7. Springer International Publishing AG.

[7] Hirulkar N. S., Jaiswal P. R., Reis P.N.B., Ferreira J.A.M. 2020. "Effect of hygrothermal aging and cyclic thermal shocks on the mechanical performance of single-lap adhesive joints". International Journal of Adhesion & Adhesives 99: 102584.

[8] Kłonica M. 2015. "Impact of Thermal Fatigue on Young's Modulus of Epoxy Adhesives". Advances in Science and Technology Research Journal 9:103–106.

[9] Kłonica M. 2016. "Comparative Analysis of Effect of Thermal Shock on Adhesive Joint Strength". Advances in Science and Technology Research Journal 10 : 263–268.

[10] Kłonica M. 2017. "Wpływ zmiennych obciążeń cieplnych na bezpieczeństwo klejonych konstrukcji lotniczych". In Bielawski R., Grenda B. (ed.) Bezpieczeństwo lotnicze w aspekcie rozwoju technologicznego. Warszawa: Wydawnictwo Akademii Sztuki Wojennej.

[11] Kłonica M., Kuczmaszewski J. 2015. „Badania porównawcze wytrzymałości na ścinanie klejowych połączeń zakładkowych stali 316L po „szokach termicznych"". Przetwórstwo Tworzyw 2: 125–130.

[12] Kubit A., Bucior M., Kluz R. 2020. "Effect of temperature on the shear strength of GFRP-aluminium alloy 2024-T3 single lap joint". Technologia i Automatyzacja Montażu 1: 30–35.

[13] Kubit A., Trzepieciński T., Kłonica M., Hebda M., Pytel M. 2019. "The influence of temperature gradient thermal shock cycles on the interlaminar shear strength of fibre metal laminate composite determined by the short beam test". Composites Part B 176 : 107217.

[14] Kuczmaszewski J., Kłonica M., Pieśko P., Zagórski I. 2015. „Klejenie w technologii szybkiego prototypowania". Mechanik 12 : 117-120.

[15] PN-EN ISO 10123:2019-07. Adhesives – Determination of shear strength of anaerobic adhesives using pin-and-collar specimens. Warsaw: Polish Committee for Standardization.

[16] PN-EN ISO 4287:1999. Specifications of product geometry - Geometric structure of the surface: profile method - Terms, definitions and parameters of the geometric structure of the surface. Warsaw: Polish Committee for Standardization.

[17] Ramalho L.D.C., Campilho R.D.S.G., Belinha J., da Silva L.F.M. 2020. "Static strength prediction of adhesive joints: A review". International Journal of Adhesion & Adhesives 96: 102451.

[18] Rojek M. 2011. Metodologia badań diagnostycznych warstwowych materiałów kompozytowych o osnowie polimerowej. Open Access Library.

[19] Rudawska A., Sikora J. W., Müller M., P. Valášek. 2020. "The effect of environmental ageing at lower and sub-zero temperatures on the adhesive joint strength". International Journal of Adhesion&Adhesives 97:102487.

[20] Szabelski J., Domińczuk J., Kuczmaszewski J. 2019. Wpływ ciepła na właściwości połączeń klejowych. Lublin: Wydawnictwo Politechniki Lubelskiej.

[21] Zielecki W., Guźla E., Bielenda P. 2020. "The Influence of Natural Seasoning on the Load Capacity of Cylindrical Adhesive Joints". Technologia i Automatyzacja Montażu 3: 15-24.

dr hab. inż. Władysław Zielecki, prof. PRz - Wydział Budowy Maszyn i Lotnictwa Politechniki Rzeszowskiej, Katedra Technologii Maszyn i Inżynierii Produkcji, al. Powstańców Warszawy 8, 35-959 Rzeszów, e-mail: wzktmiop@prz.edu.pl

dr inż. Przemysław Bielenda - Wydział Budowy Maszyn i Lotnictwa, Katedra Technologii Maszyn i Inżynierii Produkcji, al. Powstańców Warszawy 8, 35-959 Rzeszów

mgr inż. Ewelina Ozga – Wydział Budowy Maszyn i Lotnictwa, Katedra Technologii Maszyn i Inżynierii Produkcji, al. Powstańców Warszawy 8, 35-959 Rzeszów, e-mail: e.guzla@prz.edu.pl

POŁĄCZENIE sił to
POCZĄTEK,
POZOSTANIE razem to
POSTĘP,
WSPÓLNA praca
to SUKCES

Wszystkim czytelnikom,
reklamodawcom oraz
autorom współtworzącym
nasze wydania
DZIĘKUJEMY za to,
że jesteście z NAMI

WYDAWNICTWO *SIGMA-NOT*

ponad **70** LAT NA RYNKU

34 TYTUŁY

129 000 PUBLIKACJI

WYGODNY DOSTĘP
DO ARTYKUŁÓW FACHOWYCH

Nowy

PORTAL INFORMACJI TECHNICZNEJ

www.sigma-not.pl

Zmieniamy się dla Ciebie